Journal of *Marine Science and Engineering*

MDPI

Article

Mechanisms of Uranium and Thorium Accumulation in the Lower Ediacaran Marine Sediments from the Upper Yangtze Platform, China: Implications for Helium Exploration

Yi Zou [1,2], Qingyong Luo [1,2,*], Huayao Zou [1,2], Jianfa Chen [1,2], Wenming Ji [3], Jin Wu [1,2], Tao Du [1,2], Xintong Liu [1,2], Zilong Fang [1,2], Wenxin Hu [1,2], Ye Zhang [4,5] and Jinqi Qiao [1,2]

1 Hainan Institute of China University of Petroleum (Beijing), Sanya 572025, China; zouyi_1996@163.com (Y.Z.); huayaozou@cup.edu.cn (H.Z.); jfchen@cup.edu.cn (J.C.); wujin209579@163.com (J.W.); dutaochn@163.com (T.D.); 2023210025@student.cup.edu.cn (X.L.); fangzilongchn@163.com (Z.F.); 2023310026@student.cup.edu.cn (W.H.); jinqi.qiao@cup.edu.cn (J.Q.)
2 College of Geoscience, China University of Petroleum (Beijing), Beijing 102249, China
3 School of Geosciences, China University of Petroleum (East China), Qingdao 266580, China; jiwenming@outlook.com
4 National Joint Engineering Research Center for Shale Gas Exploration and Development, Chongqing Institute of Geology & Mineral Resources, Chongqing 401120, China; zhangye_sg@vip.163.com
5 Key Laboratory of Shale Gas Exploration, Ministry of Natural Resources, Chongqing Institute of Geology & Mineral Resources, Chongqing 401120, China
* Correspondence: qingyong.luo@cup.edu.cn

Abstract: The ocean is a significant global reservoir of uranium (U) and thorium (Th). These elements can be incorporated into marine sediments through processes involving organic matter (OM), redox conditions, terrigenous inputs, and mineral interactions. Helium generated through the radioactive decay of U and Th within geological formations represents a critical potential resource. Marine black shales, which are rich in U and Th, are widespread in the Ediacaran Doushantuo Formation of the Upper Yangtze Platform, making them a key target for helium exploration. However, there is limited research on the mechanisms behind U and Th accumulation in these shales. This study focuses on shales from the Doushantuo Formation in Chongqing, China, aiming to explore the mechanisms of U and Th accumulation and assess the potential for helium generation, and argillaceous dolomites are included for comparative analysis. The results show that the average U and Th content in the black shales (17.58 and 9.78 ppm, respectively) is higher than that of argillaceous dolomites (3.52 and 2.75 ppm, respectively). Uranium mainly comes from authigenic precipitation and hydrothermal inputs, while thorium is primarily sourced from terrigenous and hydrothermal inputs. The semi-humid climate in the provenance area facilitated parent rock weathering, with atmospheric precipitation and river systems transporting U and Th to the ocean. However, excessive terrigenous input can dilute the U and Th content in the sediments. In the shales, uranium is primarily adsorbed and/or complexed by organic matter (OM), with the anoxic–euxinic sedimentary environment and high OM content (TOC = 0.06–34.58 wt.%, r = 0.95) promoting U accumulation. Thorium accumulation is largely controlled by adsorption onto clay minerals. The total amount of helium generated from the Doushantuo shales is estimated to be 7.20×10^{10} m^3.

Keywords: helium exploration; uranium accumulation; thorium accumulation; marine black shales; Ediacaran; Doushantuo formation

Academic Editor: Timothy S. Collett

Received: 7 February 2025
Revised: 20 February 2025
Accepted: 20 February 2025
Published: 23 February 2025

Citation: Zou, Y.; Luo, Q.; Zou, H.; Chen, J.; Ji, W.; Wu, J.; Du, T.; Liu, X.; Fang, Z.; Hu, W.; et al. Mechanisms of Uranium and Thorium Accumulation in the Lower Ediacaran Marine Sediments from the Upper Yangtze Platform, China: Implications for Helium Exploration. *J. Mar. Sci. Eng.* **2025**, *13*, 413. https://doi.org/10.3390/jmse13030413

1. Introduction

The ocean is one of the largest reservoirs of uranium (U) and thorium (Th) on Earth, with an estimated total amount in the billions of tons, far exceeding the known reserves of these elements on land [1]. The concentrations of U and Th in seawater have remained relatively stable, with U levels typically around 3 ppb (parts per billion) and Th concentrations ranging between 0.03 and 0.06 ppb [2–4]. These elements in the ocean primarily originate from terrigenous sources [5]. Atmospheric precipitation and river systems transport U and Th from land to the ocean, where they are eventually deposited in marine sediments [6,7].

Helium is a unique gas that is colorless, odorless, chemically inert, and has a low boiling point (4.22 K at standard temperature and pressure) [8]. It is a natural resource with strategic value and is widely used in high-tech industries and scientific research, such as aerospace, nuclear industries and cryogenics [9,10]. Pure helium gas reservoirs have not been discovered worldwide, as helium is typically found in association with natural gas [9]. As a result, the extraction of helium from natural gas reservoirs containing helium remains the primary method for industrial helium production [9–11]. However, owing to the increasing demand for helium (at an annual rate of 4–6%), the global reserves and production of helium are becoming increasingly limited [12,13]. The United States (40%), Qatar (19%), Algeria (16%), Russia (13%) and Canada (4%) collectively account for over 90% of global estimated helium resources, totaling approximately 51.9 billion cubic meters in 2017 [10,12–14]. Given current consumption rates, these reserves are projected to be depleted in about 230 years [15]. In addition, limited helium resources have been discovered in China, representing only 2% of global estimated helium resources (1.1 billion cubic meters) in the world [10]. However, China's annual consumption exceeds 25.7 million cubic meters, with over 80% dependent on imports [16]. This makes helium resource exploration in China essential, as the country is facing a shortage of helium.

Helium has two stable isotopes, ^{3}He and ^{4}He. ^{3}He mainly comes from mantle degassing ($^{3}He/^{4}He \approx$ 1–30 Ra, contrasting with crustal values of <0.02 Ra, Ra = atmospheric $^{3}He/^{4}He$ ratio of 1.4×10^{-6}), whereas ^{4}He mainly comes from the decay of radioactive elements ^{238}U, ^{235}U, and ^{232}Th [17]. The main sources of helium in sedimentary basins are atmospheric helium, crustal helium (radioactive helium), and mantle-derived helium [8,18]. Atmospheric helium has little effect on helium concentration in gas reservoirs. The sources of helium in global gas fields that can be used for industrial production are mantle-derived helium and crustal helium [19]. Mantle-derived helium consists mainly of helium stored in the mantle during the early stages of Earth's formation [10]. Mantle-derived helium is characterized by an enrichment of ^{3}He ($^{3}He/^{4}He \geq 6$ Ra) and can be transported into shallow crustal fluids via magmatism and faults, along with other gases, such as CO_2, N_2, and CH_4 [10,20]. Crustal helium (^{4}He) is usually found in natural systems in trace amounts, and helium concentrations higher than those in the air (5.24 ppm) are commonly discovered in groundwater and gas reservoirs [15].

The amount of helium produced in the crust directly depends on the age of the helium source rocks and the average U and Th contents in the rocks and minerals [8]. Thus, ancient U–Th-rich rocks are favored for helium formation. Marine black shales are rich in U and Th, and are generally recognized as major sources of crustal helium [15,18]. The average U contents in shale range from 4 to 60 ppm [21–23], and the average Th content in shale is 12 ppm [24,25]. For example, the Cambrian Niutitang Formation shale exhibit extreme U enrichment (up to 122 ppm) due to euxinic conditions, and the average Th content in the shales is approximately 10 ppm [26]. U and Th accumulation in shale is influenced mainly by organic matter (OM), redox conditions, terrigenous input, and minerals [21,27–29]. OM is capable of adsorbing and/or complexing U, but different types of OM have distinct U contents [21]. For example, algae-derived amorphous OM adsorbs up to 550 ppm U,

whereas terrestrial OM binds < 50 ppm U due to lower surface functional groups [21,28]. U–Th-bearing minerals, such as zircon, monazite and apatite, in shales contain significant U and Th contents (e.g., monazite: Th up to 300,000 ppm) [30]. The geochemical properties of U and Th differ during deposition, and Th is more stable than U. The stability and mobility of U are strongly influenced by its oxidation state [28]. Naturally occurring U is primarily composed of U (IV) and U (VI), wit h U (IV) being substantially less soluble than U (VI) [31]. U (VI) migrates more easily in oxidizing environments [32,33]. Other valence states of U (U (0), U (III), and U (V)) are almost unstable [28,34–36]. Th is usually insoluble in water, less active during low-temperature geological processes, and easily preserved in stable Th-bearing minerals. Th is transported mainly by terrigenous input and can be enriched in weathering residues [37]. Additionally, Th can migrate as organic complexes or colloids under suitable conditions [38,39].

The Upper Yangtze Platform contains abundant helium resources, and helium reservoirs have been found in the Weiyuan and Jinqiu gas field, where the average helium concentrations are 0.2% and 0.07%, respectively [40,41]. However, the distribution of helium resources is complex, and the helium production capacity is quite different in this area [40,42]. The black shale of the Ediacaran Doushantuo Formation is widespread, indicating potential helium source rocks [43]. However, there are limited studies on the mechanism of U and Th accumulation in the Doushantuo Shales. In this work, shales and argillaceous dolomites from the Doushantuo Formation in the Upper Yangtze Platform are collected, and the argillaceous dolomites are used as comparative samples to investigate the mechanism of U and Th accumulation in marine sediments. This study aims to provide guidance for helium exploration and alleviate the shortage of helium resources.

2. Geological Setting

The Yangtze Platform runs from the western to eastern China, and the platform includes mainly Sichuan, Chongqing, Guizhou, Hubei, Anhui, and Jiangsu Provinces, with an area of approximately 500,000 km^2 (Figure 1A). The Yangtze Platform is one of the ancient platforms in China with abundant hydrocarbon resources [44]. The main exploration area of the Doushantuo Formation studied in this paper is located in the northeast and southeast of Chongqing, China (Figure 1B).

The Doushantuo Formation was deposited on top of the Nantuo Formation glacial deposits, with thicknesses ranging from 0 to 420 m (Figure 2A) [45]. The Doushantuo Formation is composed of four members, namely, Z_1d_1, Z_1d_2, Z_1d_3, and Z_1d_4, from the bottom to the top (Figure 2A) [43], and the formation consists mainly of grey argillaceous dolomite, micritic dolomite, and black shale (Figure 2A–C) [46]. The paleogeography of the Doushantuo Formation was influenced mainly by paleouplifts and marginal sags (Figure 1C–E) [43]. In the study area, the paleogeography exhibited by Z_1d_1 was dominantly shore and shallow-water shelf environments, and the paleogeography exhibited by Z_1d_2 was dominantly shallow-water shelf and deep-water shelf-basin environments (Figure 1C,D) [43]. Z_1d_3 exhibits dominantly mixed shelf and shallow-water shelf environments, with enhanced oxic conditions in the sedimentary environment. Z_1d_4 is absent or was not deposited in most parts of the Sichuan paleouplift, except for the marginal sags and shelfs of western Hubei Province [43]. The Z_1d_1 cap dolomite was deposited mainly along the margin of the Sichuan Basin [45]. The primary lithology of Z_1d_2 is black shale, and the primary lithologies of Z_1d_3 are dolomite and argillaceous dolomite (Figure 2A–C). Z_1d_2 and Z_1d_3 formed during a transgressive–regressive cycle (Figures 1D,E and 2A) [43,46]. The primary lithology of Z_1d_4 is black shale (Figure 2A), which was formed during a transgressive–regressive cycle, along with the overlying massive carbonates of the Dengying Formation (Figure 2A) [45]). In the marginal sags, such as the Chengkou and Hefeng

sags, the average thicknesses of the source rocks are greater than 50 m (Figure 1F) [47], and the average total organic carbon (TOC) contents are generally greater than 2.0 wt.% [43]. On the other hand, in the Xiushan area, the average thicknesses of organic-rich shale range from 30 to 50 m (Figure 1F) [48], and the average TOC contents are usually greater than 1.0 wt.% [43].

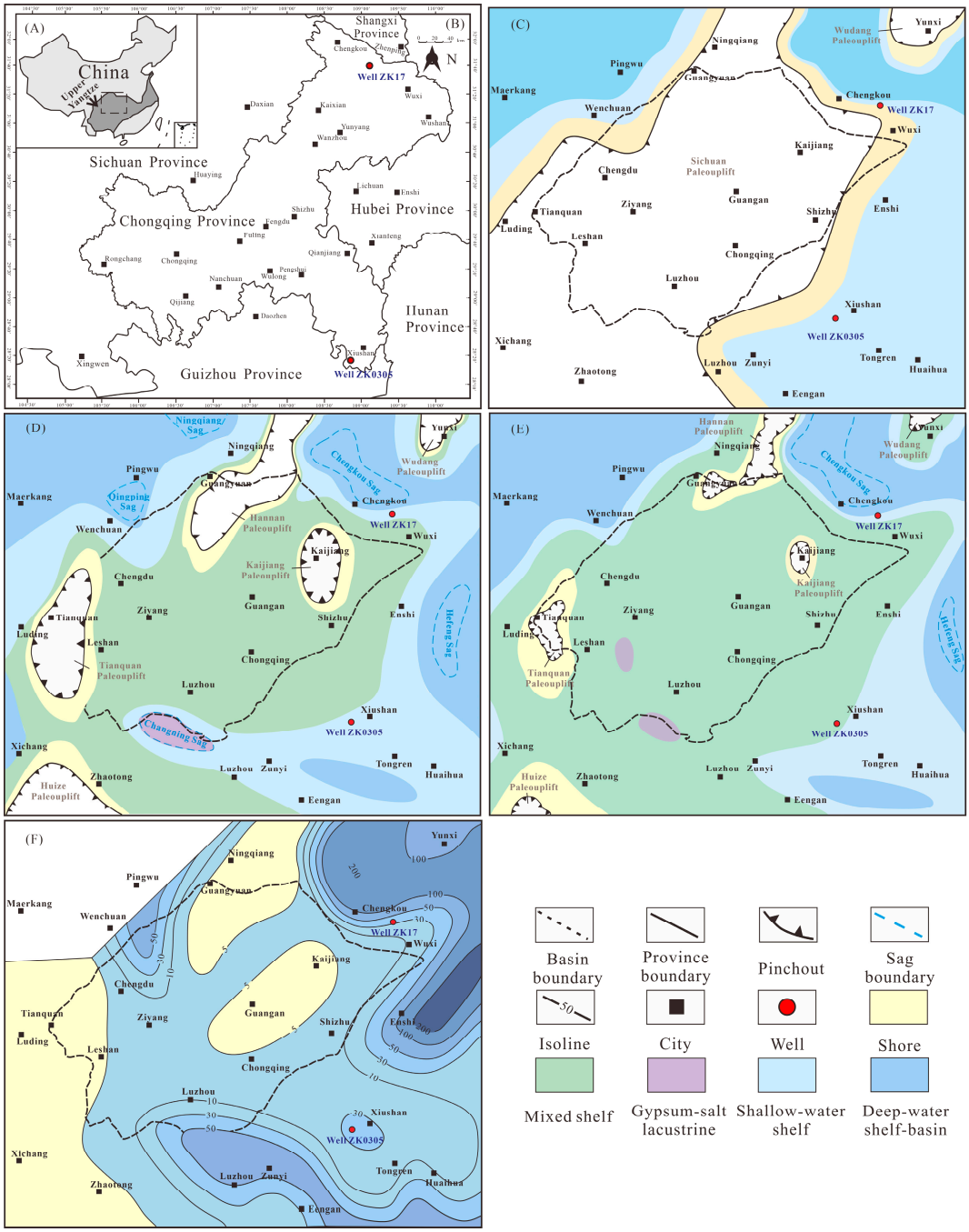

Figure 1. (**A**) Location of the study area in South China; (**B**) location map of Chongqing, showing sample sites. Modified from the work of Luo, et al. [49]. (**C**) Paleogeography of the Z_1d_1 in the Upper Yangtze Platform; (**D**) paleogeography of the Z_1d_2 in the Upper Yangtze Platform; (**E**) paleogeography of the Z_1d_3 in the Upper Yangtze Platform; (**F**) spatial variation in shale thickness of the Doushantuo Formation in the Upper Yangtze Platform. Figure (**C**–**F**) was modified from the work of Wang, Liu, Jiang, Huang, Wang, Xu, Jiang, Shi, Ren and Wang [43].

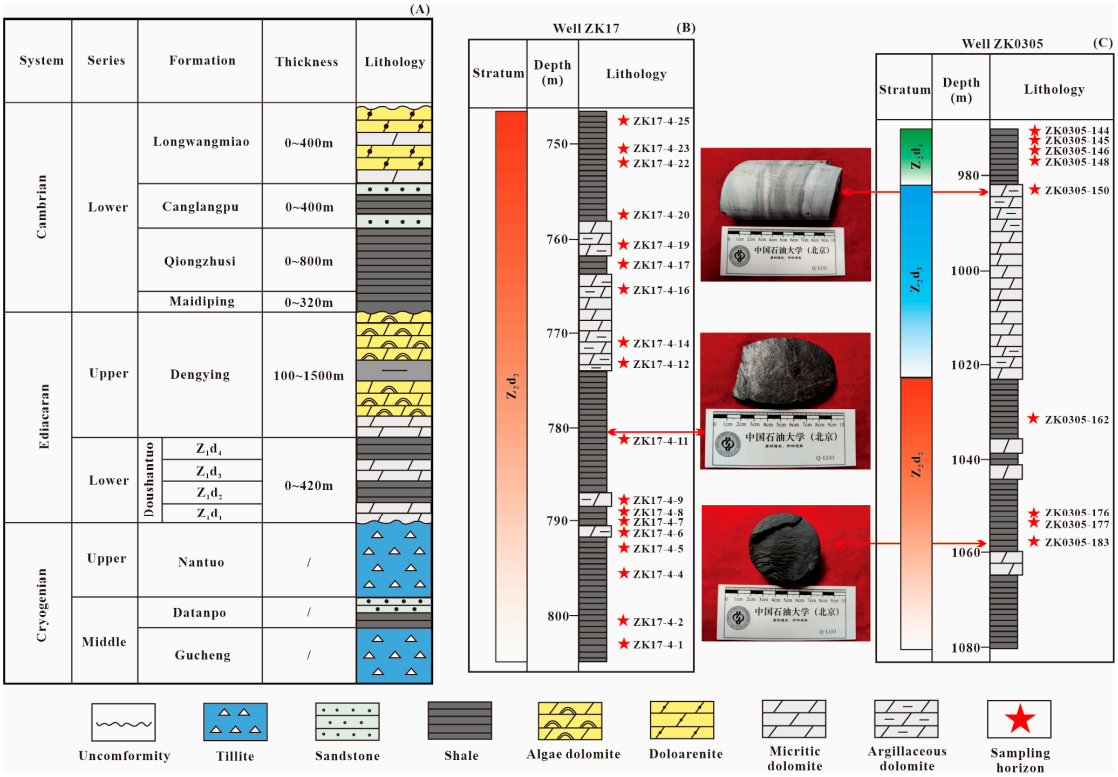

Figure 2. (**A**) Cryogenian–Cambrian stratigraphic column in the Upper Yangtze Platform (modified from Xiao, Cao, Luo, Tan, Xiao, He and Li [45]), as well as the stratigraphic columns of the Doushantuo Formation in the (**B**) well ZK17 and (**C**) well ZK0305. Note: "/" indicates "unknown".

3. Sampling and Methods

3.1. Samples

A total of 27 Doushantuo Formation core samples were collected for this study; these samples included 13 black shales and 5 argillaceous dolomites from well ZK17 in Chengkou, Chongqing, and 8 black shales and 1 argillaceous dolomite from well ZK0305 in Xiushan, Chongqing (Figures 1B and 2B,C). The sampling intervals of the shales were generally of less than 7 m, while only a few argillaceous dolomites were collected for comparison purposes.

3.2. Organic Petrography

These fresh samples were ground to 200 mesh size. The powdered samples were processed with diluted HCl, and the residues were washed with distilled water more than 30 times and then dried. The TOC content was measured via a Leco CS-230 (Leco Corporation, St. Joseph, MI, USA). The core samples were cut into small blocks of 2 cm × 2 cm × 1 cm, which were subsequently cured with epoxy resin and dried. The smooth surfaces of the blocks were subsequently obtained by grounding and polishing via an EcoMet 250 machine (Buehler Ltd., Lake Bluff, IL, USA) with an AutoMet 250 (Buehler Ltd., Lake Bluff, IL, USA). Microscopic observations and in-source solid bitumen reflectance measurements were conducted on a Leica DM4500 (Leica Microsystems GmbH, Wetzlar, Germany) microscope equipped with a CRAIC photometer and a 50× oil immersion objective. Strontium titanate (R_o = 5.36%), cubic zirconia (R_o = 3.08%), and gadolinium–gallium–garnet (R_o = 1.725%) were used as standard materials to calibrate the reflectance measurements. The experiments were performed at the National Key Laboratory of Petroleum Resources and Engineering, China University of Petroleum (Beijing).

3.3. Mineral Analysis

The mineralogical composition of the powdered samples was determined via X-ray diffraction (XRD), which was performed on a Bruker D2 Phaser (Billerica, MA, USA). The quantitative analysis of mineral components was performed via the Chinese standard procedure SY/T5163-2010 [50]. The rock samples were cut into small pieces and polished with sandpaper and argon ions. Then, they were coated with carbon for scanning electron microscope microscopy (SEM) analysis. The mineral distribution and composition were examined via a Zeiss Sigma 500 field emission SEM instrument (Oberkochen, Germany), equipped with an X-ray energy-dispersive spectrometry (EDS) instrument. XRD analyses were performed at the National Key Laboratory of Petroleum Resources and Engineering, China University of Petroleum (Beijing), and SEM analyses were performed at the National Research Center for Geoanalysis of the China Geological Survey.

3.4. Elemental Analysis

The concentrations of major and trace elements were analyzed at the Institute of Geochemistry, Chinese Academy of Sciences. A 50 mg powdered sample was blended with 1 mL of 38% HF and 2 mL of 68% HNO_3 in a polytetrafluoroethylene (PTFE) bomb. The container was then sealed and heated at 190 °C for 12 h. After cooling, 2 mL of HNO_3, 0.5 μg of Rh (as an internal standard), and 5 mL of deionized water were added, and the mixture was heated at 135 °C for 5 h. The sample was diluted with deionized water to a concentration of 1/3000th of the original concentration and tested via inductively coupled plasma–mass spectrometry (ICP–MS). Andesite, plagioclase gneiss, and slate were used as standards. The ICP–MS analysis achieved an accuracy better than ±5–10%. Sample preparation for major elements was similar to that for trace elements, with an internal standard of 1 mL of 10 ppm Cd (except for SiO_2). The treated solution was diluted 1000 times and tested via inductively coupled plasma–optical emission spectroscopy (ICP–OES). For SiO_2, 0.25 g of NaOH and 0.05 g of the powdered sample were added to a silver crucible and heated at 700 °C for 30 min. After cooling, deionized water was added, and the mixture was heated. After the products were dissolved, 5 mL of HCl was added, followed by the addition of deionized water to a solution volume of 250 mL. ICP–OES was also used to test the diluted solution. The loss on ignition (LOI) values was determined by calculating the mass difference before and after heating 1 g of the powdered sample at 900 °C for 1 h. The error of ICP–OES error for the elements was less than ±5%.

3.5. Data Presentation

The enrichment factor (EF) is calculated by the following equation: $X_{EF} = (X/Al)_{sample}/(X/Al)_{PAAS}$ [51], in which, X is the target element and PAAS is Post-Archean Australian Shale [52].

The chemical index of alteration (CIA), chemical index of weathering (CIW) and plagioclase index of alteration (PIA) can serve as proxies for the reconstruction of the paleoclimate and weathering degree of the parent rock and are calculated as follows: $CIA = [Al_2O_3/(Al_2O_3 + CaO^* + Na_2O + K_2O)] \times 100$, $CIW = [Al_2O_3/(Al_2O_3 + CaO^* + Na_2O)] \times 100$, and $PIA = [(Al_2O_3 - K_2O)/((Al_2O_3 - K_2O) + CaO^* + Na_2O] \times 100$ [53–55]. CaO* is the percentage of CaO in silicate minerals. The McLennan, et al. [56] correction method ($CaO' = CaO - 10/3 \times P_2O_5$), which assumes that silicate material has reasonable Ca/Na ratios, was used. CaO* equals the smaller of the values between those of CaO′ and Na_2O. Generally, the CIA values range from 50 to 100, with different CIA values representing different climatic and weathering conditions: cold and arid climates and low chemical weathering (CIA = 50–60), warm and humid climates and intermediate chemical

weathering (CIA = 60–80), and hot and humid climates and extreme chemical weathering (CIA = 80–100) [53].

Trace elements (e.g., U) in marine shales are usually composed of terrigenous inputs (transported or particulate) and the authigenic fraction. It is often assumed that authigenic U can be approximately calculated by the difference between the bulk concentration and detrital fraction ($U_{authigenic} = U_{bulk} - U_{bulk} \times Al_{bulk}/Al_{PAAS}$) [52,57].

Eu anomalies can be utilized to determine the presence of hydrothermal influences in marine deposits [58]. Eu anomalies are calculated as follows: $\delta Eu = Eu_{PAAS}/(Sm_{PAAS} \times Gd_{PAAS})\hat{}0.5$, in which, X_{PAAS} represents the PAAS-normalized concentration of element X [52].

In order to quantitatively evaluate the helium generation of the Doushantuo Formation black shale on the Upper Yangtze Platform, a calculation formula for the amount of helium generation is established based on the formula proposed by Ballentine and Burnard [17]: $V_{He} = (1.207 \times 10 - 13 \times [U] + 2.868 \times 10 - 16 \times [Th]) \times \rho_r \times S_S \times h_S \times yr$, where V_{He} represents the volume of helium produced by the shale (m^3), [U] denotes the concentration of U in the shale (ppm), [Th] is the content of Th in the shale (ppm), yr denotes the age of the shale (years), ρ_S is the density of the shale (assumed to be 2.65 t/m^3), S_r is the distribution area of the shale (m^2), and h_S means the thickness of the shale (m).

4. Results

4.1. Organic Petrographic Characteristics

The primary maceral constituents of the shales are in-source solid bitumen, which appears grayish white when viewed under reflected light (Figure 3) [59,60]. Abundant in-source solid bitumen with heterogeneous distribution can be observed in the shales from the ZK17 well (Figure 3A,B). However, OM is more dispersed in the ZK0305 well sample (Figure 3F–I). Pyrite filled with OM can be observed in the shales (Figure 3C–E). The reflectance values of the in-source solid bitumen in ZK17 and ZK0305 obtained in the random direction are between 2.62% and 2.96% and between 3.01% and 4.52%, respectively. According to the formula developed by Luo, Zhang, Zhong, Wu, Goodarzi, Sanei, Skovsted, Suchý, Li, Ye, Cao, Liu, Min, Pan, Yao and Wu [59], the maturity values of the ZK17 are between 2.53% and 2.83%, and those of ZK0305 are between 2.86% and 4.29%, indicating that the OM in the Doushantuo Formation is in the overmature stage.

4.2. Geochemistry

4.2.1. TOC

The shales displayed a wide variation in TOC values, ranging from 0.06 to 34.58 wt.% (Table S1), with an average of 6.47 wt.%. The shales from well ZK17 have a higher average TOC content of 6.85 wt.% than those from well ZK0305 (Table S1). The ZK17-4-1 sample has the highest TOC content of 34.6 wt.% and is a sample of an abundant in-source solid bitumen, as shown in Figure 3A,B. The TOC contents of samples ZK0305-162 and ZK0305-176 are notably lower than those of the other shales, at 0.06 wt.% and 0.08 wt.%, respectively (Table S1). The argillaceous dolomites have an average TOC content of 0.98 wt.%, with a range of 0.05 to 2.87 wt.% (Table S1). The variable range of TOC in the shales and dolomites indicates the heterogeneity of the OM distribution in the Doushantuo Formation.

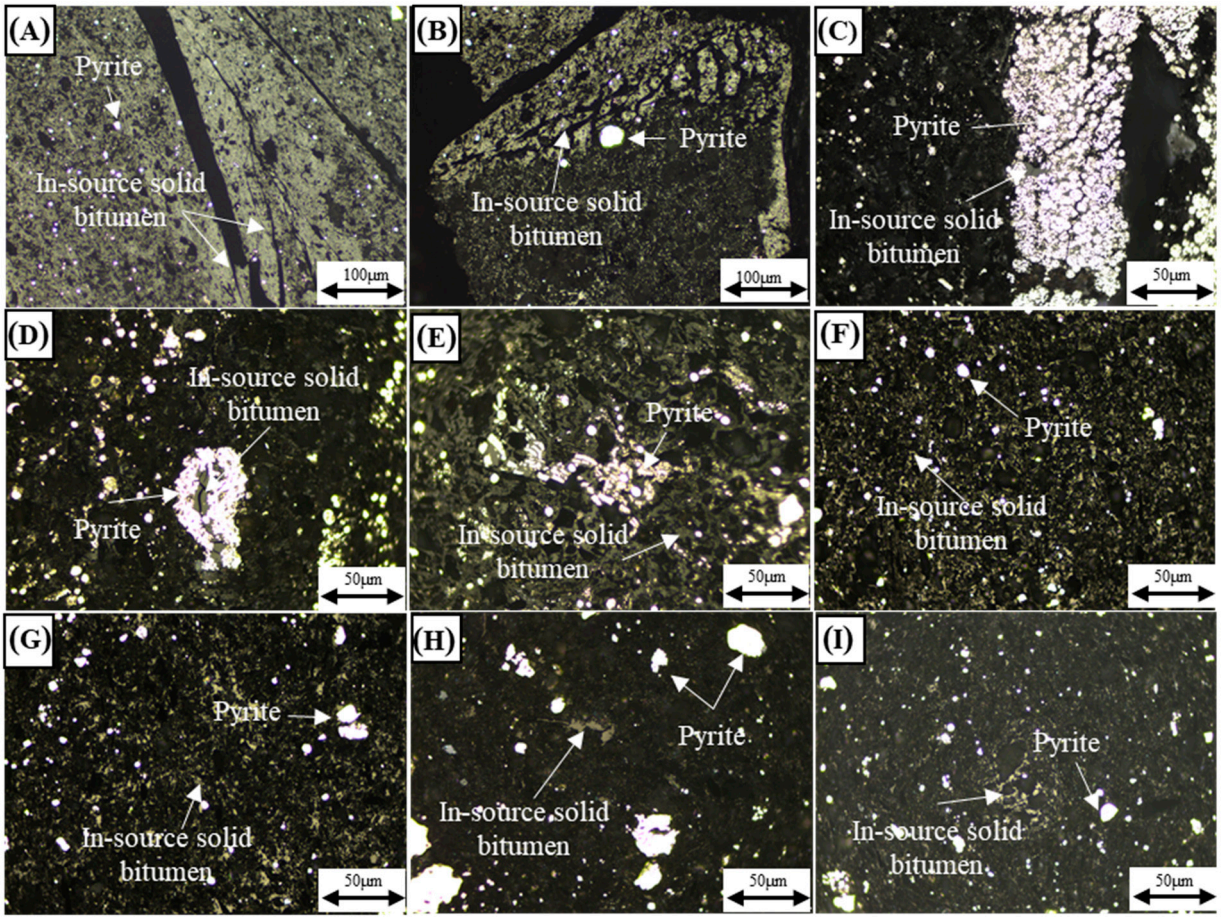

Figure 3. Photomicrographs of in-source solid bitumen and pyrite in reflected white light and oil immersion. (**A**,**B**) from ZK17-4-1, TOC is 34.58 wt.%; (**C**,**D**) from ZK17-4-3; TOC is 9.48 wt.%; (**E**) from ZK17-4-4; (**F**) from ZK0305-144; (**G**) from 0305-145; (**H**,**I**) from ZK0305-146, TOC is 6.18 wt.%; (**C**–**E**) have the phenomenon that pyrite filling OM.

4.2.2. Major Elements

The average concentrations of major elements in the shales are 56.7 wt.% for SiO_2, 11.6 wt.% for Al_2O_3, 5.5 wt.% for Fe_2O_3, 2.5 wt.% for MgO, 4.0 wt.% for CaO, 1.2 wt.% for Na_2O, 3.4 wt.% for K_2O, 0.2 wt.% for MnO, 0.7 wt.% for TiO_2, and 1.3 wt.% for P_2O_5 (Table S1). The samples have higher average concentrations of MgO, CaO, Na_2O, MnO, and P_2O_5 and lower concentrations of SiO_2, Al_2O_3, Fe_2O_3, K_2O, and TiO_2 than those of the post-Archean Australian shale (PAAS; Figure 4A) [52]. The argillaceous dolomites contain 32.2 wt.% SiO_2, 3.1 wt.% Al_2O_3, 1.8 wt.% Fe_2O_3, 7.7 wt.% MgO, 15.5 wt.% CaO, 0.3 wt.% Na_2O, 1.0 wt.% K_2O, 10.3 wt.% MnO, 0.2 wt.% TiO_2, and 0.3 wt.% P_2O_5. These dolomites have higher average concentrations of MgO, CaO, and MnO and lower concentrations of the other elements than post-Archean Australian shale (PAAS) (Figure 4B) [52].

4.2.3. Trace Elements

The shales contain an average of 17.58 ppm U and 9.78 ppm Th, and the argillaceous dolomites have averages of 3.52 ppm U and 2.75 ppm Th, which are much lower than those in the shales (Table S1). All trace elements obtained were normalized to PAAS (Figure 5) [52]. On average, the shales and argillaceous dolomites are enriched in U and depleted in Th compared with PAAS (Figure 5A,B).

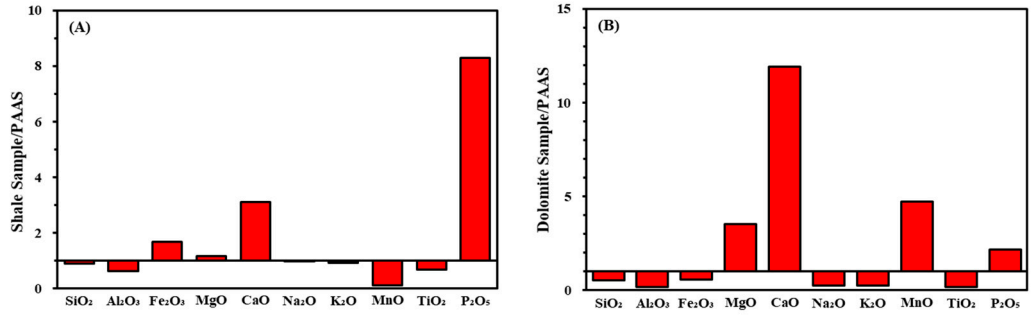

Figure 4. PAAS-normalized [52] Taylor and McLennan, 1985; (**A**) major element diagrams for the Doushantuo Shales; (**B**) major element diagrams for the Doushantuo argillaceous dolomites.

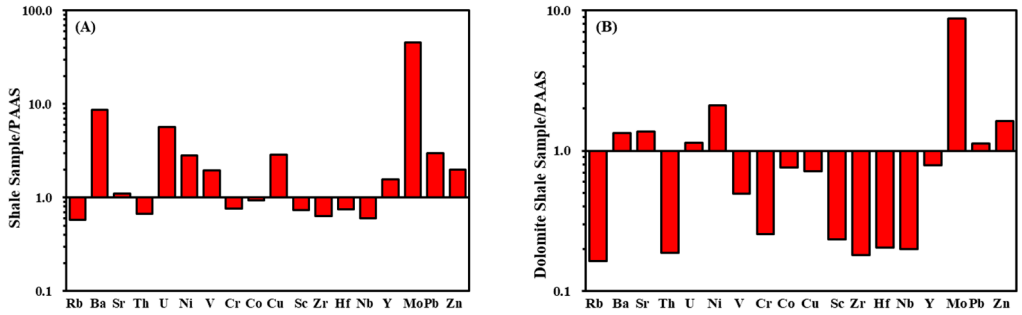

Figure 5. PAAS-normalized [52]; (**A**) trace element diagrams for the shales; (**B**) trace element diagrams for the argillaceous dolomites.

For the redox-sensitive trace elements, the average Mo, V, Pb, Zn, Cu, and Ni contents in the shales are greater than those in PAAS (Figure 5A). Th correlates poorly with redox-sensitive trace elements, and U has moderate positive correlations with V, Cr, Zn, Cu, Ni, and Pb in shales (Table S2; r = 0.67, 0.81, 0.71, 0.72, 0.55, and 0.54, respectively). The average Mo, Pb, and Zn contents in the argillaceous dolomite are relatively high compared with those in PAAS, and the average contents of V, Ni, and Cu are lower than those in PAAS. The U and Th contents in the argillaceous dolomite do not show any correlation with other mostly redox-sensitive elements (Table S3).

4.2.4. Minerals in the Shale

The shales mainly comprise quartz, clay minerals, dolomite, and iron–dolomite, and the argillaceous dolomites mainly comprise dolomite and ankerite, along with some manganite, siderite, pyrite, hematite, calcite, feldspar, and clay minerals (Table S1, Figures 6 and 7). Quartz is the most common mineral in shale, with an average content of 29.9 wt.% (Table S1). The quartz content of argillaceous dolomites (mean of 11.5 wt.%) is lower than that of shales (mean of 29.9 wt.%; Table S1). Quartz appears grayish-white under the SEM, and it is predominantly irregular with angular, semi-angular, or subrounded shapes, with crystal sizes ranging from micrometers to nanometers (Figure 7B–D,F). Clay minerals are another common mineral in shale, with an average content of 32.9 wt.%. However, the argillaceous dolomites contain lower clay mineral contents than shales, averaging 10.1 wt.%. Under SEM, micron-sized elongated illite can be observed (Figure 7A). The average percentages of dolomite and ankerite in the shales are 10.9 wt.% and 1.6 wt.%, respectively. In the argillaceous dolomite, the average percentages of dolomite and ankerite are 27.4 wt.% and 26.1 wt.%, respectively, which are much greater than those in the shales (Table S1 and Figure 6). Fe^{2+} can replace Mg^{2+} in the dolomite lattice to form ankerite. As an isomorphic phase of dolomite, ankerite has similar optical properties and crystal structures [61]. Both dolomite and ankerite appear grayish white in color under SEM (Figure 7G,H). The average pyrite content in the shales is 6.4 wt.%, and the average pyrite

content in argillaceous dolomites is 5.1 wt.% (Table S1 and Figure 6). The pyrite in the sample is mainly euhedral pyrite and framboidal pyrite (Figures 3 and 7C,D). Rhodochrosite is present in four argillaceous dolomites, with an average content of 19.1 wt.% (Table S1 and Figure 6). The barite content is low, at less than 1 wt.%. Sphalerite is not detectable in the XRD analysis but is observable via SEM (Figure 7F). Because of the presence of heavy elements, the secondary and backscattered electron images of sphalerite and barite are very bright (Figure 7E,F). Small quantities of these minerals are observable only via SEM (Figure 7A,C) within the shales. A higher apatite content is observable in sample ZK4-16, with a content of 13.5 wt.% (Table S1 and Figure 6). SEM–EDS reveals that the dominant form of apatite in the shale is chlorapatite, which has an irregular shape (Figure 7C). Zircons are dispersed mainly in granular form with small particle sizes (less than 5 μm) and appear grayish-white (Figure 7A).

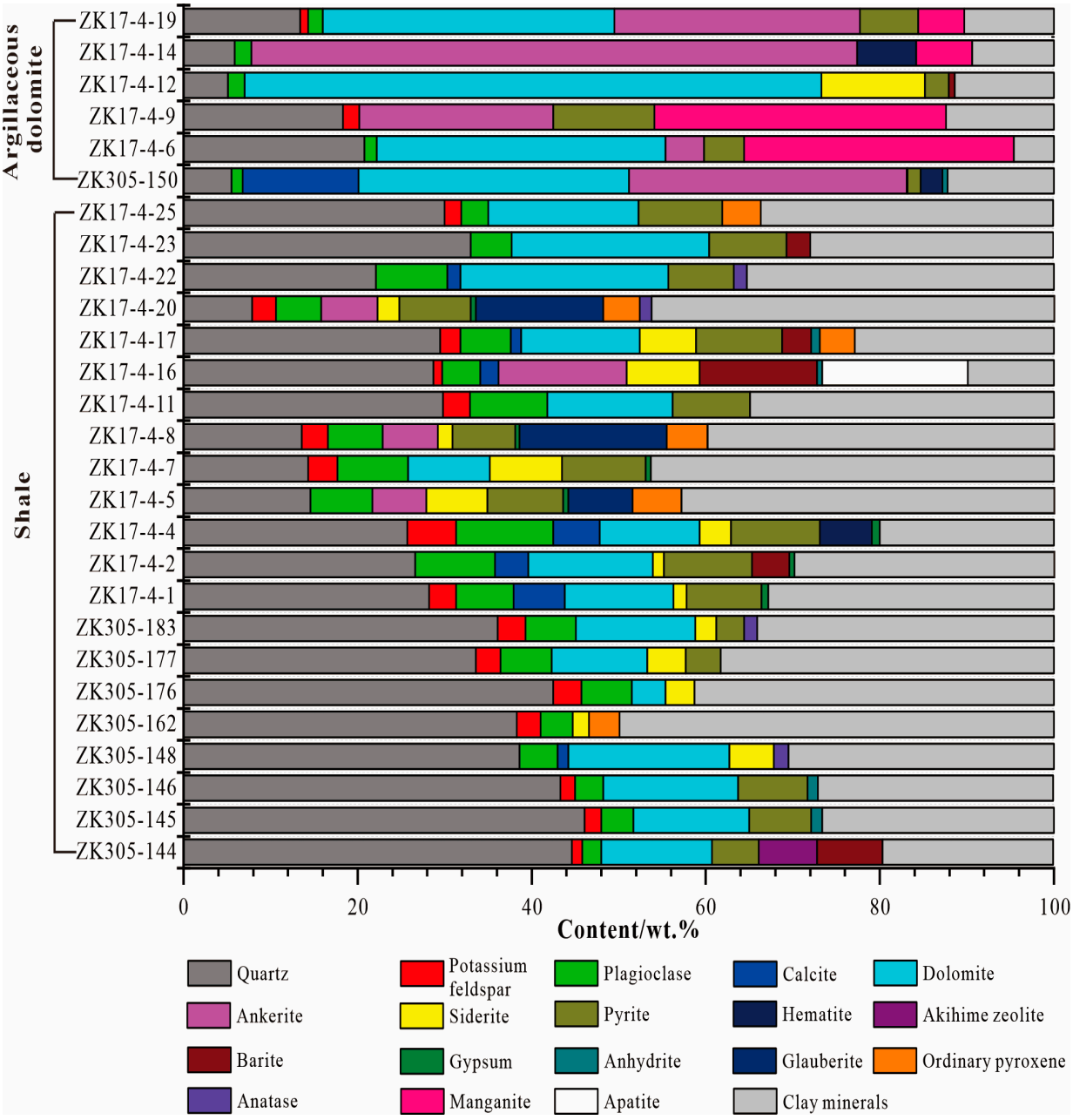

Figure 6. The mineral composition of shales and argillaceous dolomites.

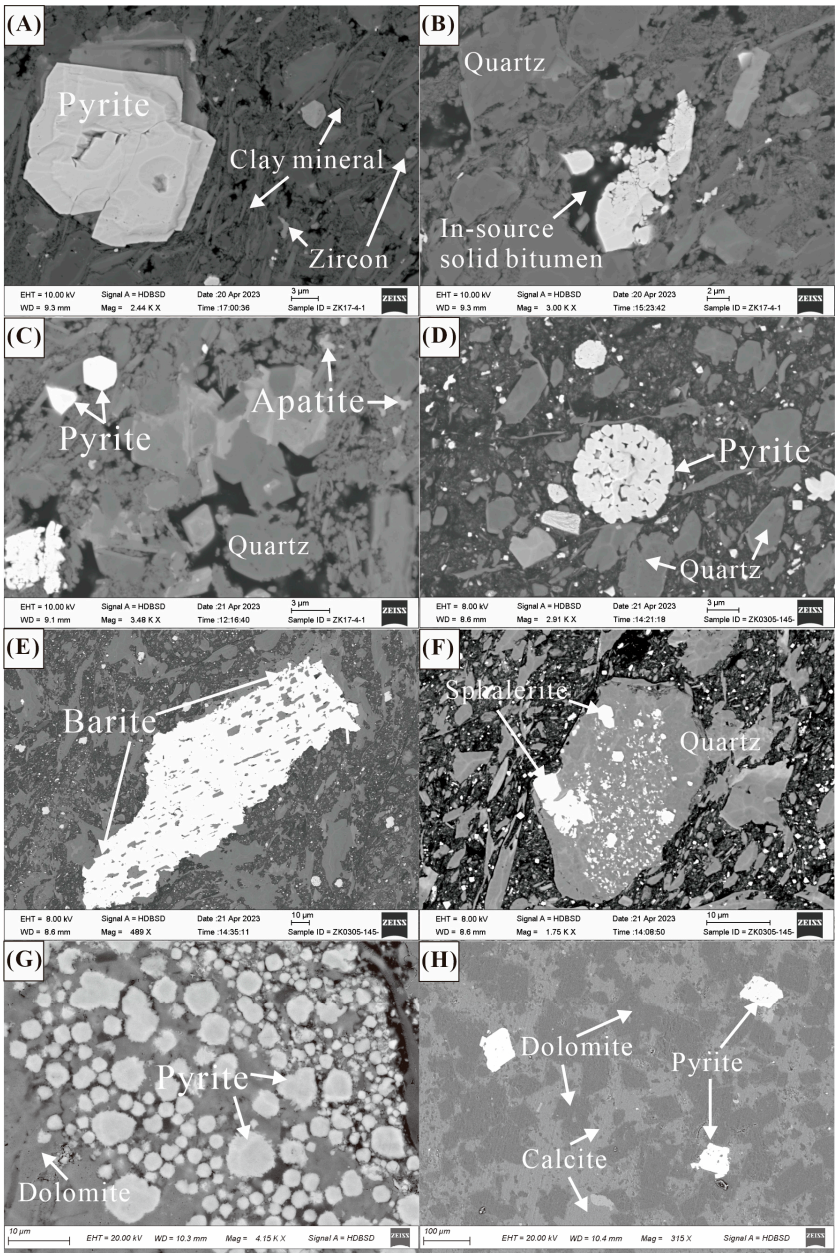

Figure 7. SEM images of minerals in shales and argillaceous dolomites in the Doushantuo Formation. (**A**–**C**) from ZK17-4-1; (**D**–**F**) from ZK0305-145; (**G**) from ZK17-4-9; (**H**) from ZK0305-150.

5. Discussion

5.1. Sedimentation Conditions and Environments

(1) Terrigenous input

In previous studies, Al, Ti, Zr and Th were commonly used to indicate terrigenous input [62]. Al and Ti are found primarily in heavy minerals and aluminosilicates, such as rutile and ilmenite [27], and remain relatively constant during diagenesis [51]. The Al_2O_3 content of the shales ranges from 2.56 to 17.7 wt.%, with an average of 11.55 wt.%, and the Ti content ranges from 636.6 to 6019.6 ppm, with an average of 4010.5 ppm (Table S1). The argillaceous dolomite has lower Al_2O_3 and Ti contents of 1.83–6.67 wt.% and 576.9–2256.0 ppm, averaging 3.11 wt.% and 1081.8 ppm, respectively (Table S1). The Al_2O_3 and Ti contents show comparable trends throughout the stratigraphic column (Figure 8A,B).

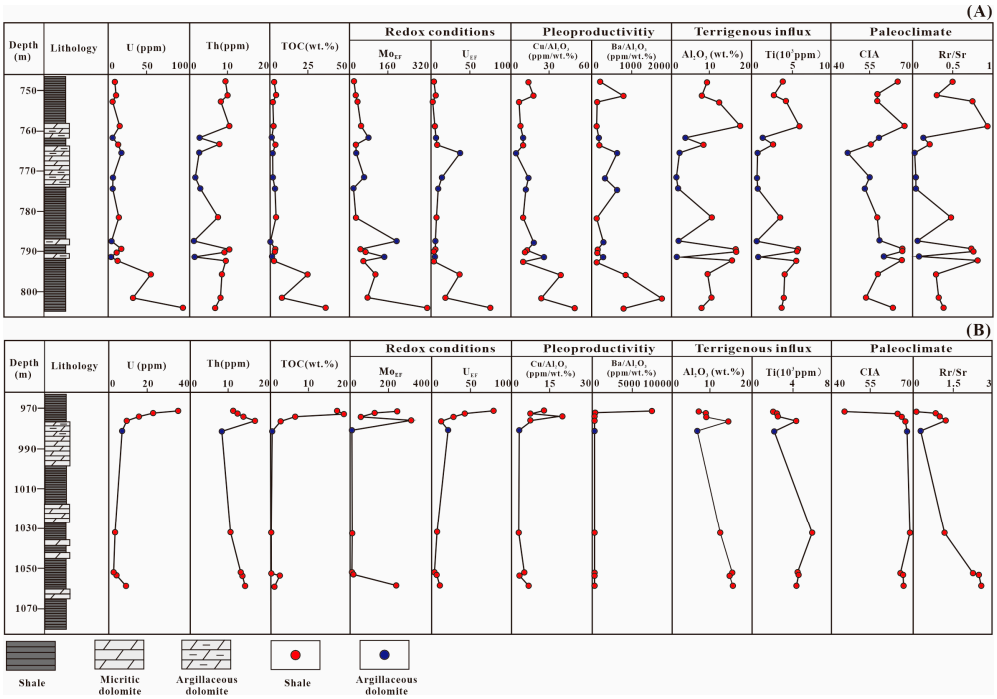

Figure 8. Stratigraphic distributions of U contents, Th contents, TOC contents, terrigenous influx, redox, paleoproductivity and paleoclimate proxies of (**A**) well ZK17 and (**B**) well ZK0305 for the Doushantuo Formation in the Upper Yangtze Platform.

(2) Redox conditions

Redox-sensitive elements, such as Mo, U, V, and Ni, and their ratios, such as Ni/Co and U/Th, can serve as paleoredox proxies [63]. As shown in Table S1, Ni/Co and U/Th in the shales are in the ranges of 1.95–35.85 (mean of 7.42) and 0.22–14.47 (mean of 2.32), respectively, and they are 2.77–8.60 (mean of 6.18) and 0.82–2.91 (mean of 1.63) in argillaceous dolomites, respectively, indicating oxic–dysoxic–anoxic depositional environments for the shales and argillaceous dolomites (Table S1 and Figure 9A) [64,65]. The enrichment of Mo and U in marine sediments is mainly controlled by the average concentrations of Mo and U in the water column, the redox state of the water column, and the hydrological characteristics of the basin [51]. U is activated in the Fe (III)-Fe (II) reduction zone and can be transferred to sediments under reducing conditions [66], whereas Mo is enriched in sediments only when seawater contains H_2S [67]. Therefore, the Mo–U covariation pattern is a practical alternative for extrapolating the redox conditions of shales [29,68]. The Mo_{EF} values of the shales range from 0.96 to 288.51, with an average of 76.45, and the U_{EF} contents range from 1.16 to 69.7, with an average of 11.44 (Table S1 and Figure 9B), indicating that anoxic–euxinic conditions characterize the redox conditions of the shales.

(3) Paleoproductivity

Cu is usually present in oxidized water as organometallic complexes, with limited Cu (II) ions [27,69]. During decomposition of the organic matter at the bottom of the seawater column, Cu is released into the pore water and adsorbed by the pyrite under anoxic conditions [70,71]; so, it can be used as an effective proxy to evaluate paleoproductivity. Ba is also widely used in paleoproductivity assessments [72,73]. Al_2O_3 is commonly used to remove the effects of terrigenous input [74]. In this study, Cu/Al_2O_3 and Ba/Al_2O_3 were employed as proxies for paleoproductivity. As shown in Table S1, the Cu/Al_2O_3 ratios of the shales range from 2.37 to 45.98 ppm/wt.%, with an average of 13.71 ppm/wt.%, and the Ba/Al_2O_3 ratios range from 94.99 to 7421.65 ppm/wt.%, with an average of 669.81 ppm/wt.%. The argillaceous dolomite has a lower Cu/Al_2O_3 and Ba/Al_2O_3 ratios of 2.68–26.05 ppm/ wt.% and 172.37–563.79 ppm/wt.%, averaging 14.97 ppm/wt.% and 301.83 ppm/wt.%, respec-

tively (Table S1 and Figure 8), indicating that the paleoproductivity of the shales is greater than that of the argillaceous dolomites [51].

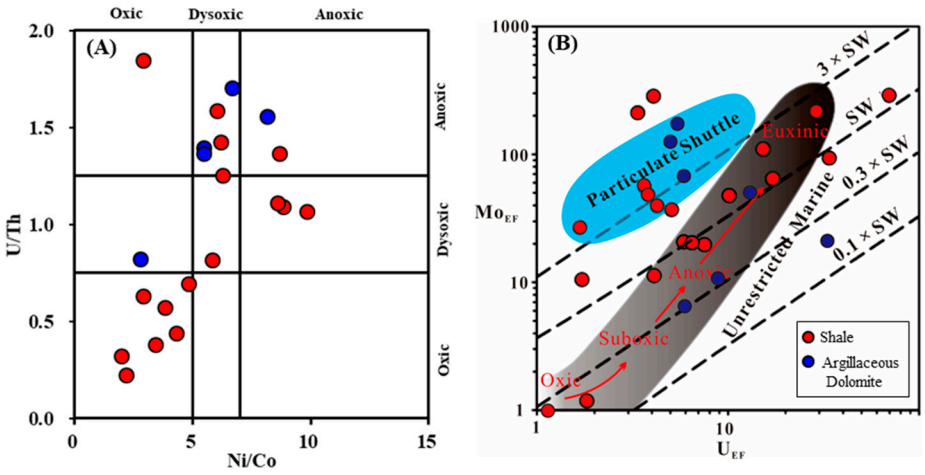

Figure 9. Covariation in (**A**) U/Th versus Ni/Co and (**B**) Mo_{EF} versus U_{EF} for the shales and argillaceous dolomites in the Upper Yangtze Platform (modified from Algeo and Tribovillard [29]).

(4) Paleoclimate and paleoweathering

The Doushantuo Formation has moderate CIA values, ranging from 44.90 to 68.91, with a mean of 60.57 (Table S1), suggesting a semi-humid climate and intermediate chemical weathering. The calculated CIW and PIA values for the Doushantuo Formation range from 51.94 to 89.18 (mean of 75.54) and 43.01–84.24 (mean of 68.44), respectively, indicating a semi-humid climate and intermediate chemical weathering during its deposition. The Rb/Sr ratio is often used to reconstruct the paleoclimatic evolution [64]. The Rb/Sr values of the Doushantuo Formation range from 0.02 to 2.60, with an average of 0.70, indicating a semi-humid climate [75].

5.2. Source of Uranium and Thorium

La/Sc and Th/Co ratios can be employed in provenance analysis as silicic rocks are enriched in La and Th and depleted in Sc and Co compared with basic rocks [50,76]. As shown in Figure 10a, the shales are derived from silicic rocks. On the basis of Hayashi, et al. [77] and Figure 10b, the samples suggest derivation from a felsic source. Wang, et al. [78] reported that Neoproterozoic sedimentary rocks are sourced mainly from Neoproterozoic magmatic rocks, which are widely distributed in the northern part of the Yangtze Platform [78,79]. Hu [80] suggested that sediments in Z_1d_1, Z_1d_2 and Z_1d_3 were derived from Neoproterozoic magmatic rocks in the northern part of the Yangtze Platform, and that sediments in Z_1d_4 were derived from the Kongling Group in the northern part of the Yangtze Platform. The Kongling Group is mainly composed of Paleoproterozoic granitic gneiss and metasedimentary rocks [81]. The CIA, CIW, PIA and Rb/Sr values indicate a semi-humid climate and intermediate chemical weathering in the provenance area (Table S1). Therefore, the parent rocks distributed in the northern part of the Yangtze platform (i.e., Neoproterozoic magmatic rocks and/or the Kongling Group) could have provided U and Th after weathering during the deposition of the Doushantuo Formation. Atmospheric precipitation can transport the weathering products of parent rocks to surficial river systems, after which the river delivers soluble U (VI) and insoluble Th-containing minerals to the ocean [5,82]. U is deposited under increasing reducing conditions and forms authigenic U in the water column and/or pore water, which accounts for 40 to 70% of the total flux of riverine U input [6,7]. Th in shales is derived mainly from terrigenous input;

however, the extremely low deposition rate of the Doushantuo Formation (≤5.6 m/Myr) was not conducive to Th accumulation because of its geochemical inertness [45].

The $U_{authigenic}$ values in the shales range from 0.52 to 52.67 ppm, with an average of 8.44 ppm, and the $U_{authigenic}$ values in the argillaceous dolomites range from 1.40 to 4.27 ppm, with an average of 2.80 ppm (Table S1). Authigenic U values range from 8% to 86% of the total U in shales, with an average of 39%, and range from 64% to 90% of the total U in argillaceous dolomites, with an average of 84% (Table S1). Zheng, et al. [83] reported that accumulation rates of authigenic U range from 20 to 70 μg/cm^2 kyr in marine sediments and that a substantial amount (one-third to two-thirds) of the authigenic U is eventually preserved in marine sediments. Therefore, authigenic U is an important source of U in the Doushantuo Formation. Owing to its geochemical inertness and insolubility, authigenic Th is usually absent in marine sediments.

Hydrothermal fluids can supply trace elements (e.g., U and Th) to lakes or the ocean [84,85]. Eu anomalies can be utilized to determine the presence of hydrothermal influences in marine deposits [58]. The δEu values of the shales range from 0.98 to 3.38, with an average of 1.20 (>1), and the δEu values of the argillaceous dolomites range from 1.12 to 1.22, with an average of 1.16 (>1, Table S1), indicating that hydrothermal input was common during the deposition of the Doushantuo Formation, which is consistent with the findings of Liu, et al. [86] and Xiao, Cao, Luo, Tan, Xiao, He and Li [45].

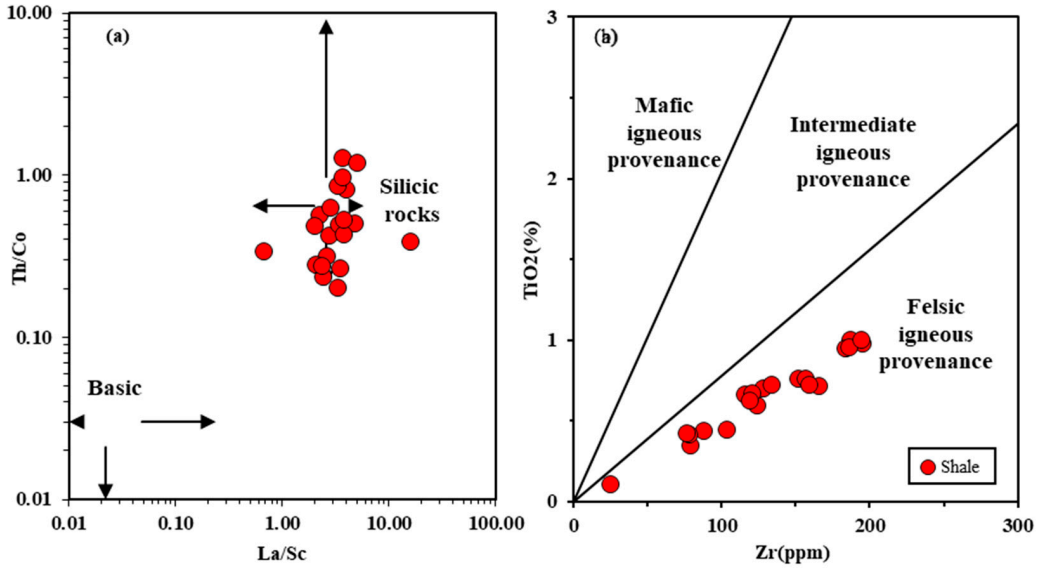

Figure 10. (**a**) Th/Co-La/Sc [87]; note that shales plot close to the silicic rock; (**b**) TiO_2-Zr [77]; note that shales plot falls into the felsic igneous provenance.

5.3. Factors Controlling Uranium Accumulation

5.3.1. Uranium and Redox Conditions

Under oxic–suboxic circumstances, uranyl carbonate complexes ($UO_2(CO_3)_3^{4-}$), which are chemically inert, are the major form of soluble U (VI) present in the oxidized sedimentary environment [7,66]. U is reduced to U (IV) under reducing conditions and is commonly in the form of insoluble authigenic U (UO_2) [35]. Particularly, under euxinic condition, U is more easily separated from the water [51]. U is positively correlated with Ni/Co and U/Th in the shales (r = 0.85 and 0.91, respectively; Figure 11A,B), demonstrating that U accumulation is controlled by redox conditions and that the reducing environment is beneficial for U accumulation.

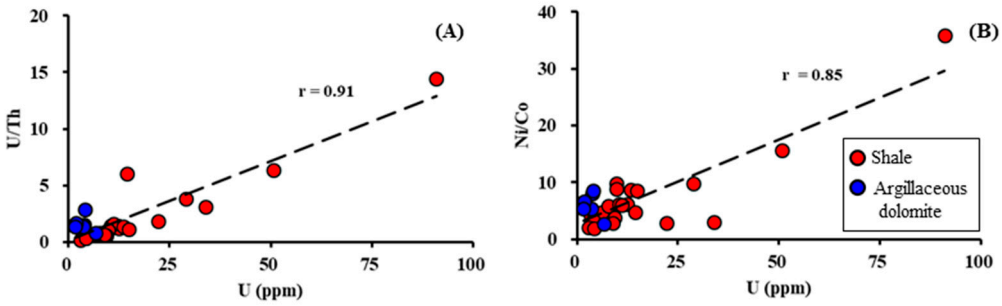

Figure 11. Cross-plots of U content versus (**A**) U/Th and (**B**) Ni/Co.

5.3.2. Uranium and Organic Matter

There are three primary forms of U in the crust: (1) independent minerals, such as uraninite and pitchblende [28]; (2) isomorphous minerals, in which U is replaced by other elements (e.g., Ca^{2+} and Zr^{4+}), forming U-bearing minerals, such as apatite [88]; and (3) dispersed adsorption state, which is a prevalent form in which U is mainly adsorbed/complexed on the surfaces of minerals and OM in rocks [89]. Independent U-bearing minerals were not found in the shales, and few isomorphous U-bearing minerals (zircon and apatite) were found (Table S1 and Figure 7). Notably, a strong positive correlation exists between the U and TOC contents in the Doushantuo Formation (r = 0.95, Figure 12A), and shale sample ZK17-4-1 has the highest TOC and U contents (Table S1). Many studies have also reported positive correlations between U and OM, such as r = 0.86 indicating the positive correlation in the U deposit located north of the Aquitaine Basin [90] and r = 0.92 indicating the positive correlation in the natural soil in the Dischma Valley [91]. OM contains aliphatic, aromatic, carboxyl, hydroxyl, phenolic, and thiosulfate functional groups that determine the solubility and bonding capabilities of OM [28]. Under reducing conditions, OM can be better preserved, and the hydroxyl or carboxyl groups in OM can adsorb (or complex) U in the water column and/or pore water to form uranyl–organometallic complexes [29,91]. Gad, et al. [92] reported that biosorption experiments of U were carried out using five kinds of local algae in Egypt, and the results revealed that the algae had a strong adsorption capacity for U. There was a poor correlation between the U and TOC contents in argillaceous dolomites (r = 0.13, Figure 12B), indicating that U may exist mainly in the inorganic phase. Authigenic U (UO_2) is the predominant form of U in argillaceous dolomite and typically coats the surfaces of clastic grains [82]. Ba/Al_2O_3 and Cu/Al_2O_3 are positively correlated with the U content (Figure 12C,D), suggesting that higher paleoproductivity is favorable for U accumulation in sediments. Liu, Mastalerz, Schieber and Teng [21] reported that U in the New Albany Shale is mainly associated with amorphous OM (average U content of ~ 550 ppm). The source of OM was dominantly lower aquatic organisms, such as algae, during the deposition of the Doushantuo Formation. However, the macerals were dominantly in-source solid bitumen in the Doushantuo Formation because of the overmature thermal maturity (Figure 3). Some U can be expelled from source rocks at percentages ranging from 43 to 48% during the process of hydrocarbon generation, as indicated by laboratory simulation experiments [93]. Thus, the oil retained in the shale also contains significant U, and the retained oil is transferred to in-source solid bitumen via thermal cracking [59], resulting in U enrichment in the in-source solid bitumen. This can also be confirmed by the fact that abundant in-source solid bitumen and a high U content are simultaneously present in shales ZK17-4-1, ZK17-4-3, and ZK17-4-4 (Figure 3A–I). The symbiosis of U and solid bitumen has also been found in carbonate-hosted U deposits in Guizhou, China, and U is thought to be derived mainly from the expelled oil [94].

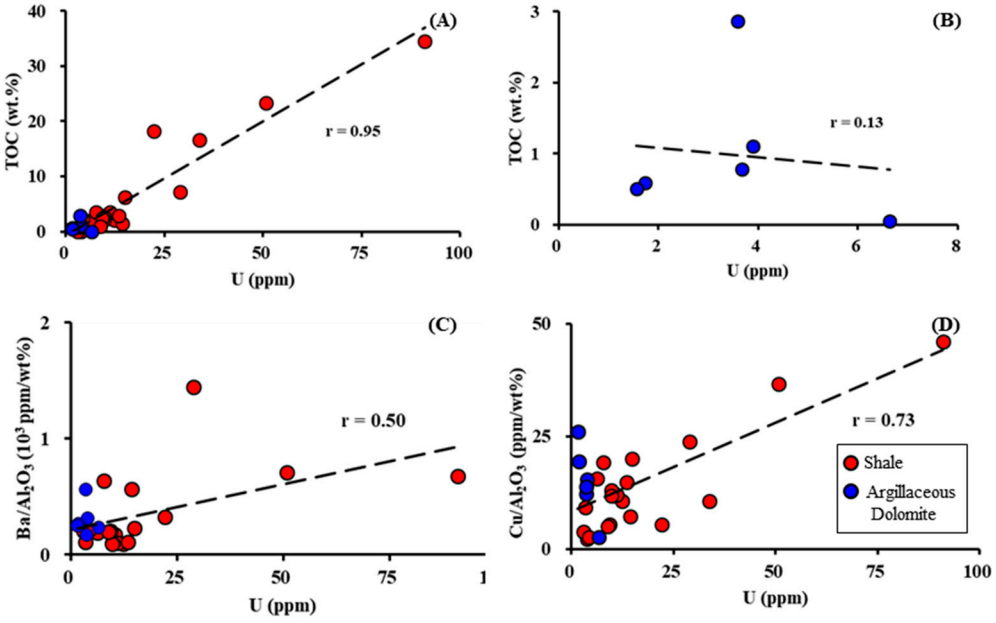

Figure 12. Cross-plots of (**A**) U versus TOC; (**B**) magnification of argillaceous dolomites in (**A**); (**C**) U versus Ba/Al_2O_3; and (**D**) U versus Cu/Al_2O_3.

5.4. Factors Controlling Thorium Accumulation

There is no apparent correlation between the Th and TOC contents in these samples (Figure 13A), suggesting that Th exists mainly in the inorganic phase rather than in OM. Th usually exists in the tetravalent form as ThO_2 and $ThSiO_4$ or in some accessory minerals (e.g., monazite and zircon) and can also be adsorbed by some minerals (e.g., hematite and clay minerals) [95,96]. Some Th-containing minerals, such as apatite and zircon, which are sourced from the terrigenous and hydrothermal inputs, can be found in shales (Figure 7A,C). The ability of clay minerals to adsorb Th (IV) has been studied under laboratory conditions [97–99]. For example, as the pH of a solution increases from 1 to 4.5, the affinity of Th to kaolinite becomes significantly greater, resulting in the formation of inorganic–cationic complexes [100]. However, Th is usually adsorbed by clay minerals in the form of small Th-containing minerals in marine sediments [101]. The clay mineral contents in the shales range from 9.9 wt.% to 49.9 wt.%, with an average value of 32.9 wt.%, and the clay mineral contents of the argillaceous dolomites range from 4.6 wt.% to 12.4 wt.%, with an average value of 10.1 wt.% (Table S1). The Th content tends to increase with increasing clay mineral content in the studied samples (Figure 13B), implying that Th is mainly distributed in the clay mineral matrix.

There are positive correlations between Th and Rb, Cs, Al_2O_3, SiO2, and KO_2 in the collected samples (Figure 13C–G). Zhao, et al. [102] reported that Rb and Cs in Jurassic No. 6 coals from the Iqe Coalfield in the Qaidam Basin, China, were adsorbed mainly by K-rich clay minerals and that the sediment was also enriched in Th. Ward, et al. [103] reported a robust Rb–K correlation in Permian coals. Rb is bound more strongly to the inorganic phase in sediments, and clay minerals have a stronger capacity for adsorbing Rb than that of OM [104]. In sediments, OM and clay minerals can adsorb Cs [102]. However, Cs is more commonly found in K-rich minerals, such as illite and montmorillonite, as it can isomerize potassium [105]. Therefore, Th, Rb, and Cs in the Doushantuo Formation may be adsorbed by K-rich clay minerals (Table S4).

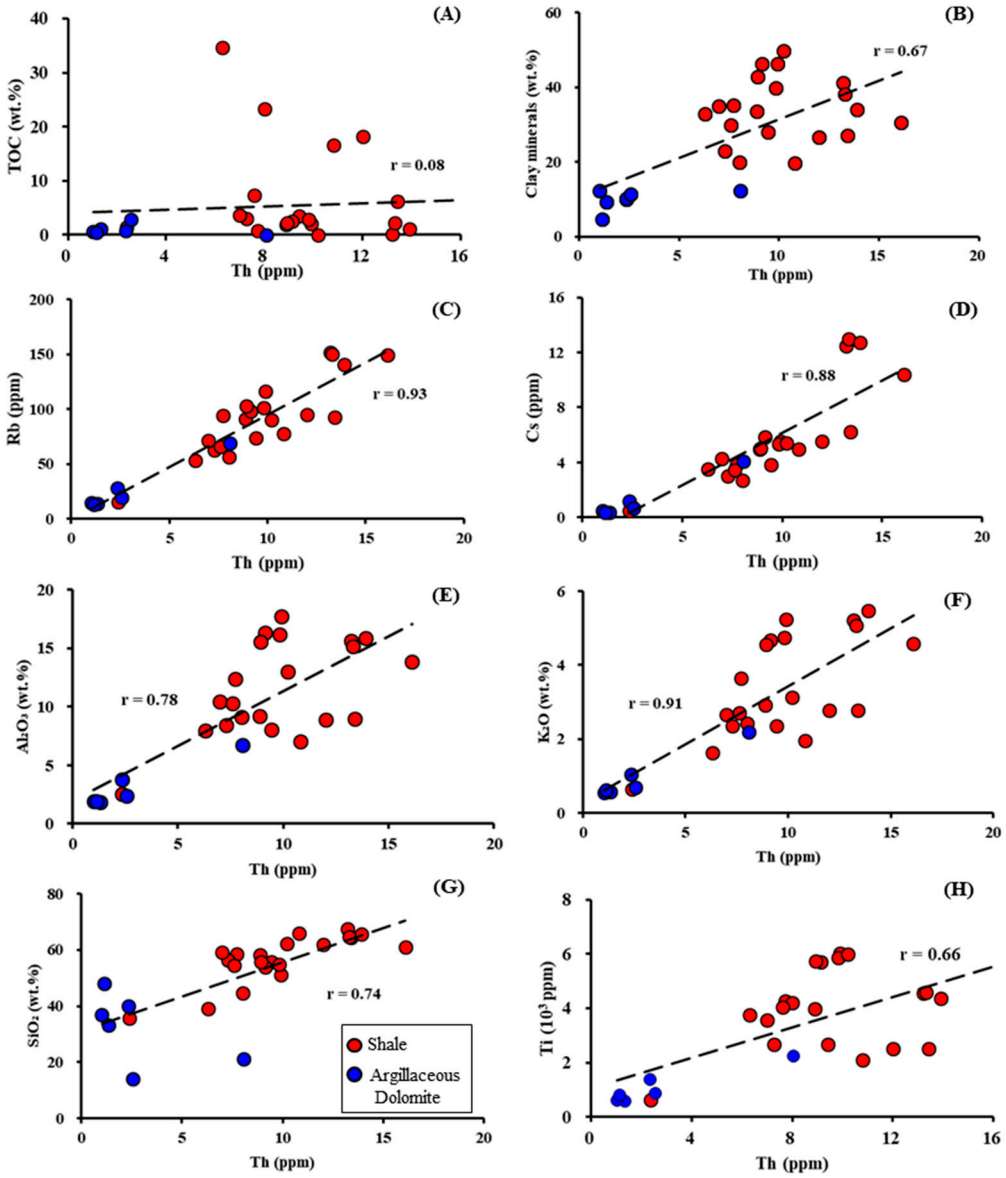

Figure 13. Cross-plots of Th content versus (**A**) TOC, (**B**) clay minerals, (**C**) Rb, (**D**) Cs, (**E**) Al_2O_3, (**F**) KO_2, (**G**) SiO_2, and (**H**) Ti content.

The positive correlations between Th and Al_2O_3 and Ti contents indicate that Th is derived mainly from terrigenous input (Figure 13E,H). An adequate supply of Th is necessary for Th accumulation in marine sediments. As mentioned earlier, Th is separated from the parent rocks (e.g., Neoproterozoic magmatic rocks and/or the Kongling Group) after weathering and transported by surficial river systems along with the terrigenous input. The average Al_2O_3 and Ti contents in well ZK17 are 8.67 wt.% and 3190 ppm, respectively, which are lower than those in well ZK0305 (11.68 wt.% Al and 3700 ppm Ti), indicating that Xiushan has more considerable terrigenous input than Chengkou. The water depth in Xiushan was shallower than in Chengkou during the sedimentation of the Doushantuo Formation because of transgression and regression of the sea [43]. Thus, Xiushan was more influenced by terrigenous input, resulting in a higher Th content in Xiushan (Table S1). However, there is a notable connection between the Th and Al_2O_3 and Ti contents in samples from Chengkou (Figure 14A,B), and weak-to-moderate correlations were observed between the Th and Al_2O_3 and Ti contents in samples from Xiushan (Figure 14C,D). These

distinct correlations suggest that excessive terrigenous input may dilute Th concentrations in the formation.

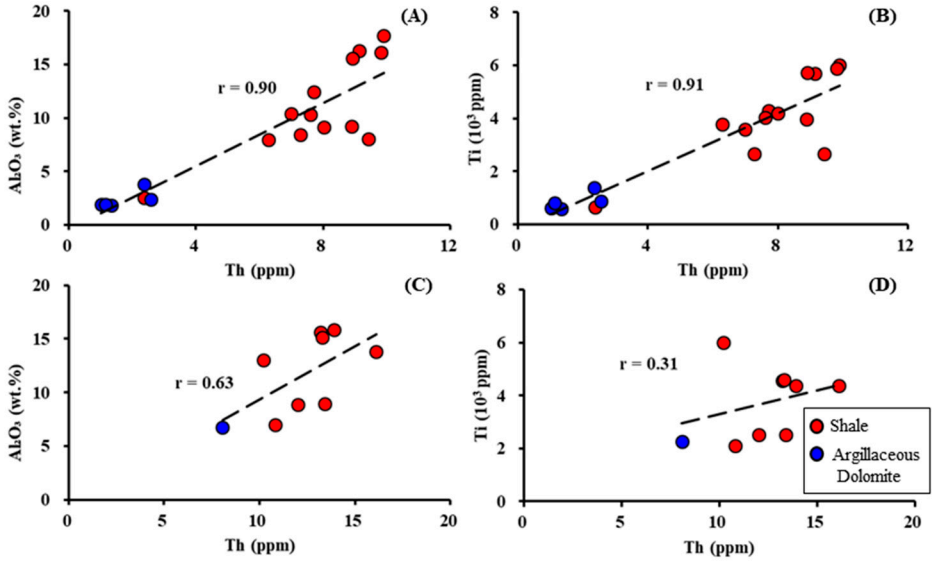

Figure 14. (**A**) Cross-plots of Th content versus Al_2O_3 content of well ZK17 samples in Chengkou; (**B**) cross-plots of Th content versus Ti content of well ZK17 samples in Chengkou; (**C**) cross-plots of Th content versus Al_2O_3 content of well ZK0305 samples in Xiushan; (**D**) cross-plots of Th content versus Ti content of well ZK0305 samples in Xiushan.

5.5. Uranium and Thorium Accumulation

The U–Th accumulation model can be established based on the above analysis and previous research on OM preservation in the Doushantuo Formation on the Upper Yangtze Platform [21,45,86,106–108] (Figure 15A–D). The surficial U and Th geochemical cycle involves several processes: weathering separates insoluble U (IV) and Th (IV) from parent rocks, oxidation converts insoluble U (IV) to soluble U (VI), atmospheric precipitation and river systems deliver soluble U (VI) and insoluble Th (IV) to the ocean, various geochemical marine processes remove U (VI) from seawater and deposit it into sediments, and Th (IV) is directly deposited in sediments (Figure 15) [5,82]. Authigenic precipitation, terrigenous input and hydrothermal input supplied the original U and Th inputs to the Doushantuo Formation (Figure 15). During the deposition of black shale in the Upper Yangtze Platform, such as in Z_1d_2 and Z_1d_4, the water depth increased due to the influence of transgression, and the reducing conditions in the depositional environment strengthened (Figure 15A,C). Many studies have reported predominantly suboxic–anoxic conditions during the deposition of the Doushantuo Formation, which is consistent with the findings of this study [45,86,106,107]. Anoxic or euxinic depositional environments can reduce dissolved U (U (VI)) to form less soluble UO_2 (U (IV)), i.e., authigenic U [7,66]. The relatively high paleoproductivity during the deposition of the Doushantuo Shales favored the preservation of OM (Table S1 and Figure 8) [45]. U dissolved in the bottom water can pass through the water–sediment surface and form uranyl–organometallic complexes in the sediments, which is beneficial for U accumulation [21,28]. In addition, a portion of U is enriched in the in-source solid bitumen that formed from the thermal cracking of the retained oil, resulting in elevated levels of U in the black shales (Figure 15D) [59]. The Th was deposited with terrigenous input and adsorbed by clay minerals in the form of small Th-containing minerals in the shales [101]. During the deposition of argillaceous dolomites, such as in Z_1d_3, the sea level fell due to tectonic movements (Figure 15B) [108]. Increased oxygen levels in the water column may have led to reactivation and redissolution of U (Figure 15D). A decrease in paleoproductivity is also not favorable for the adsorption of U

by OM (Table S1 and Figure 8). For Th, the low terrigenous input and low clay mineral content in the argillaceous dolomite results in a low Th content (Table S1, Figures 6 and 8). The Z_1d_2 and Z_1d_4 were deposited in the main depositional periods of the black shales in the study area [43], with higher U–Th contents than the Z_1d_3 dolomites. The Z_1d_2 black shale is more widely distributed and thicker than the Z_1d_4 black shale is, indicating that Z_1d_2 is a potential helium source in the Upper Yangtze Platform.

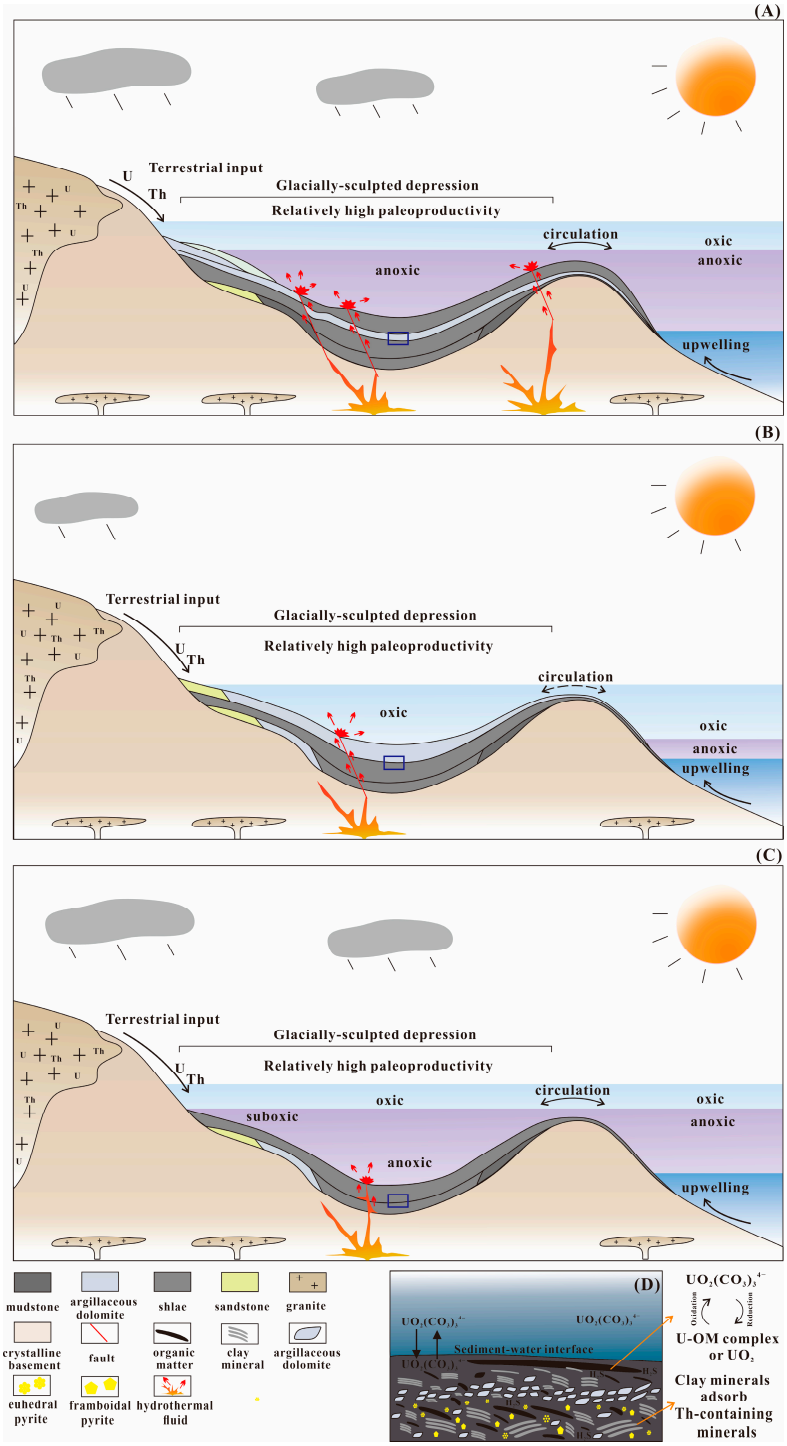

Figure 15. A model of the sedimentary evolution and U-Th accumulation model of the Doushantuo Formation in the Upper Yangtze Platform; (**A**) sedimentary evolution of Z_1d_4; (**B**) sedimentary evolution of Z_1d_3; (**C**) sedimentary evolution of Z_1d_2 (modified from Xiao, Cao, Luo, Tan, Xiao, He and Li [45]); and (**D**) U and Th micro accumulation patterns; the boxes in Figure (**A**–**C**) represent Figure (**D**).

5.6. Helium Production Potential from Black Shale

Shale rich in U and Th has a greater capacity of helium generation than that of granite and carbonate rock [24]. Helium has been found in the shale gas of the Wufeng-Longmaxi Formation in the Sichuan Basin, China, with concentrations ranging from 0.015 to 0.13% (mean of 0.039%) [109]. It is universally thought that the helium in shale gas tends to be primarily formed through the decay of the U and Th contained in the shale [10]. The average of U and Th contents in the Wufeng-Longmaxi shales is 10.4 ppm and 15.1 ppm [110–113], and the average of U and Th contents in the Doushantuo shales is 17.58 ppm and 9.78 ppm, respectively. The age of the Doushantuo Formation ranges from 635 to 560 Ma, which is older than the Wufeng–Longmaxi Formation (444 Ma). Thus, the Doushantuo shales have a great helium-generating capacity. Meng, et al. [114] found a relatively high content of helium (1.2%) in the shale gas of the Doushantuo Formation, which meets the criteria in industrial extraction. The $^{3}He/^{4}He$ ratios in the shale gas ranging from 0.009 to 0.010 Ra (Ra = 1.4×10^{-6}) indicate that the helium in the shale gas is predominantly of crustal origin, which is mainly formed by the decay of U and Th in the shale.

The average age of the Doushantuo Formation is estimated to be 5.98×10^{8} years (560–635 Ma). The shale distribution area of the Doushantuo shales in the Upper Yangtze Platform is 4.02×10^{11} m^2, and the average thickness of shale is 46.5m [47,115]. Applying the cited helium generation formula, the total amount of helium (^{4}He) generated over the course of the geological history in the Doushantuo shales is calculated to be 7.12×10^{10} m^3. Accordingly, the Doushantuo shales exhibit a considerable potential for helium production. Meanwhile, the potential for helium resource exploration can also be seen as significant in the Doushantuo shale gas.

6. Conclusions

(1) The average U and Th concentrations in black shales (17.58 ppm and 9.78 ppm, respectively) are significantly higher than those in argillaceous dolomites (3.52 ppm and 2.75 ppm, respectively). The average values of CIA (60.57), CIW (75.54), PIA (68.44) and Rb/Sr (0.70) suggest a semi-humid climate and intermediate chemical weathering in the provenance area. Atmospheric precipitation and river systems can deliver soluble U (VI) and insoluble Th (IV) into the ocean, but excessive terrigenous input may dilute the U and Th contents in the formation. The high proportion of authigenic U in the total U content—39% in shales and 84% in argillaceous dolomites—indicates that authigenic U is a significant source of U in the Doushantuo Formation. In addition, the average δEu values in shales (1.20) and argillaceous dolomites (1.16) indicate that hydrothermal input was prevalent during the deposition of the Doushantuo Formation, contributing both U and Th to the system.

(2) The positive correlation between U and TOC (r = 0.95) indicates that U in black shale is mainly adsorbed and/or complexed by OM (such as in-source solid bitumen). A relatively high abundance of OM benefits U accumulation (TOC = 0.06–34.58 wt.%). Redox conditions control the reduction in U (VI) and U adsorption and complexation by organic matter, as indicated by the positive relationships between U content and U/Th and Ni/Co ratios (r = 0.91 and 0.85, respectively). The Th accumulation mechanism differs from that of U, and it is mainly controlled by clay minerals, evidenced by a positive correlation between Th content and clay minerals (r = 0.67).

(3) The Doushantuo shales exhibit a higher potential for helium production than argillaceous dolomites due to their higher U and Th concentrations. Therefore, the Doushantuo shale gas is a promising target for helium resource exploration. The total amount of helium generated in the Doushantuo Shales is estimated to be 7.12×10^{10} m^3.

Supplementary Materials: The following supporting information can be downloaded at: https://www.mdpi.com/article/10.3390/jmse13030413/s1, Table S1: Chemical and mineral compositions of the Doushantuo Formation in the Upper Yangtze Platform; Table S2: Correlation coefficients of U content, Th content and major element content, trace element content, and TOC in shales; Table S3: Correlation coefficients of U content, Th content and major element content, trace element content, and TOC in argillaceous dolomites; Table S4: The contents of clay minerals in the shales.

Author Contributions: Conceptualization, Y.Z. (Yi Zou), Q.L., H.Z., J.C. and W.J.; Methodology, Y.Z. (Yi Zou); Investigation, Y.Z. (Yi Zou), J.W., T.D., X.L., Z.F., W.H., Y.Z. (Ye Zhang) and J.Q.; Resources, Q.L., H.Z., J.C. and W.J.; Data curation, Y.Z. (Yi Zou); Writing—original draft, Y.Z. (Yi Zou); Writing—review & editing, Y.Z. (Yi Zou), Q.L., J.W., T.D., X.L., Z.F., W.H., Y.Z. (Ye Zhang) and J.Q.; Visualization, Y.Z. (Yi Zou); Supervision, Q.L., H.Z., J.C. and W.J.; Project administration, Q.L., H.Z., J.C. and W.J.; Funding acquisition, Q.L. All authors have read and agreed to the published version of the manuscript.

Funding: This work was supported by the National Key Research and Development Program of China (No. 2021YFA0719000), National Natural Science Foundation of China (No. 42122016) and the Opening Foundation of Key Laboratory of Shale Gas Exploration, Ministry of Natural Resources (KLSGE-202201).

Institutional Review Board Statement: Not applicable.

Informed Consent Statement: Not applicable.

Data Availability Statement: The data are presented in the Supplementary Materials.

Acknowledgments: The authors wish to thank the anonymous reviewers for providing constructive comments and suggestions that substantially improved the quality of the original manuscript. Thanks to the National Key Laboratory of Petroleum Resources and Engineering, China University of Petroleum (Beijing), the Institute of Geochemistry, Chinese Academy of Sciences and the National Research Center for Geoanalysis of China Geological Survey for technical support and experimental analysis.

Conflicts of Interest: The authors declare no conflict of interest.

References

1. Xie, Y.; Liu, Z.; Geng, Y.; Li, H.; Wang, N.; Song, Y.; Wang, X.; Chen, J.; Wang, J.; Ma, S. Uranium extraction from seawater: Material design, emerging technologies and marine engineering. *Chem. Soc. Rev.* **2023**, *52*, 97–162. [CrossRef] [PubMed]
2. Moore, W.S. The thorium isotope content of ocean water. *Earth Planet. Sci. Lett.* **1981**, *53*, 419–426. [CrossRef]
3. Sackett, W.M.; Potratz, H.A.; Goldberg, E.D. Thorium content of ocean water. *Science* **1958**, *128*, 204–205. [CrossRef] [PubMed]
4. Ud-Din Khan, S.; Ahmad, A.; Khan, R.; Haneklaus, N. Uranium resources associated with phosphoric acid production and water desalination in saudi arabia. *Front. Earth Sci.* **2024**, *12*, 1341059. [CrossRef]
5. Dunk, R.M.; Mills, R.A.; Jenkins, W.J. A reevaluation of the oceanic uranium budget for the holocene. *Chem. Geol.* **2002**, *190*, 45–67. [CrossRef]
6. Barnes, C.; Cochran, J. Uranium removal in oceanic sediments and the oceanic u balance. *Earth Planet. Sci. Lett.* **1990**, *97*, 94–101. [CrossRef]
7. Klinkhammer, G.P.; Palmer, M.R. Uranium in the oceans: Where it goes and why. *Geochim. Cosmochim. Acta* **1991**, *55*, 1799–1806. [CrossRef]
8. Chen, J.; Liu, K.; Dong, Q.; Wang, H.; Luo, B.; Dai, X. Research status of helium resources in natural gas and prospects of helium resources in china. *Nat. Gas Geosci.* **2021**, *32*, 1436–1449. (In Chinese) [CrossRef]
9. Liu, K.; Chen, J.; Fu, R.; Wang, H.; Luo, B.; Dai, X.; Yang, J. Discussion on distribution law and controlling factors of helium-rich natural gas in weiyuan gas field. *J. China Univ. Pet. Ed. Natrual Sci.* **2022**, *46*, 12–21. (In Chinese) [CrossRef]
10. Wang, X.; Liu, Q.; Liu, W.; Li, X.; Tao, C.; Li, X.; Zhao, D.; Zhang, J.; Zhu, D.; Meng, Q.; et al. Helium accumulation in natural gas systems in chinese sedimentary basins. *Mar. Pet. Geol.* **2023**, *150*, 106155. [CrossRef]
11. Zhang, W.; Li, Y.H.; Zhao, F.H.; Zhou, Z.; Han, W.; Zhou, J.L.; Zhang, Q. Granite is an effective helium source rock: Insights from the helium generation and release characteristics in granites from the north qinling orogen, china. *Acta Geol. Sin. Engl. Ed.* **2020**, *94*, 114–125. [CrossRef]

12. Anderson, S.T. Economics, helium, and the U.S. Federal helium reserve: Summary and outlook. *Nat. Resour. Res.* **2018**, *27*, 455–477. [CrossRef]
13. Provornaya, I.V.; Filimonova, I.V.; Eder, L.V.; Nemov, V.Y.; Zemnukhova, E.A. Prospects for the global helium industry development. *Energy Rep.* **2022**, *8*, 110–115. [CrossRef]
14. Danabalan, D.; Gluyas, J.G.; Macpherson, C.G.; Abraham-James, T.H.; Bluett, J.J.; Barry, P.H.; Ballentine, C.J. The principles of helium exploration. *Pet. Geosci.* **2022**, *28*, petgeo2021-2029. [CrossRef]
15. Danabalan, D. Helium: Exploration Methodology for a Strategic Resource. Ph.D. Thesis, Durham University, Durham, UK, 2017.
16. Zhang, Y.; Tang, J.; Niu, Y.; Zhou, J.; Li, Y.; Wei, J. Global helium industry chain analysis and implications for china. *Preprints* **2024**. [CrossRef]
17. Ballentine, C.J.; Burnard, P.G. Production, release and transport of noble gases in the continental crust. In *Noble Gases in Geochemistry and Cosmochemistry*; Porcelli, D., Ballentine, C.J., Wieler, R., Eds.; Mineralogical Soc Amer & Geochemical Soc: Chantilly, VA, USA, 2002; Volume 47, pp. 481–538. [CrossRef]
18. Brown, A. Origin of helium and nitrogen in the panhandle-hugoton field of texas, oklahoma, and kansas, united states. *AAPG Bull.* **2019**, *103*, 369–403. [CrossRef]
19. Ballentine, C.J.; Lollar, B.S. Regional groundwater focusing of nitrogen and noble gases into the hugoton-panhandle giant gas field, USA. *Geochim. Cosmochim. Acta* **2002**, *66*, 2483–2497. [CrossRef]
20. Xu, S.; Nakai, S.i.; Wakita, H.; Wang, X. Mantle-derived noble gases in natural gases from songliao basin, china. *Geochim. Cosmochim. Acta* **1995**, *59*, 4675–4683. [CrossRef]
21. Liu, B.; Mastalerz, M.; Schieber, J.; Teng, J. Association of uranium with macerals in marine black shales: Insights from the upper devonian new albany shale, illinois basin. *Int. J. Coal Geol.* **2020**, *217*, 103351. [CrossRef]
22. Galindo, C.; Mougin, L.; Fakhi, S.; Nourreddine, A.; Lamghari, A.; Hannache, H. Distribution of naturally occurring radionuclides (U, Th) in timahdit black shale (Morocco). *J. Environ. Radioact.* **2007**, *92*, 41–54. [CrossRef]
23. Fertl, W.H.; Chilingar, G.V. Total organic carbon content determined from well logs. *SPE Form. Eval.* **1988**, *3*, 407–419. [CrossRef]
24. Brown, A.A. Ps Formation of High Helium Gases: A Guide for Explorationists (Poster Presentation). AAPG Convention, New Orleans, Louisiana. 2010. Available online: http://www.searchanddiscovery.com/documents/2010/80115brown/ndx_brown.pdf (accessed on 31 July 2018).
25. Turekian, K.K.; Wedepohl, K.H. Distribution of the elements in some major units of the earth's crust. *Geol. Soc. Am. Bull.* **1961**, *72*, 175–192. [CrossRef]
26. Tong, Z.; Zhang, J.; Ou, G.; Li, Z.; Wang, D.; Wu, Y.; Li, X.; Chen, S. Uranium enrichment driven by paleomarine condition and event deposition: Insights from the lower cambrian niutitang formation organic-rich shales in northeastern guizhou, south china. *Mar. Pet. Geol.* **2024**, *167*, 106976. [CrossRef]
27. Calvert, S.E.; Pedersen, T.F. Geochemistry of recent oxic and anoxic marine sediments: Implications for the geological record. *Mar. Geol.* **1993**, *113*, 67–88. [CrossRef]
28. Cumberland, S.A.; Douglas, G.; Grice, K.; Moreau, J.W. Uranium mobility in organic matter-rich sediments: A review of geological and geochemical processes. *Earth Sci. Rev.* **2016**, *159*, 160–185. [CrossRef]
29. Algeo, T.J.; Tribovillard, N. Environmental analysis of paleoceanographic systems based on molybdenum–uranium covariation. *Chem. Geol.* **2009**, *268*, 211–225. [CrossRef]
30. Luo, Q.; Zhong, N.; Qin, J.; Li, K.; Zhang, Y.; Wang, Y.; Ma, L. Thucholite in mesoproterozoic shales from northern north china: Occurrence and indication for thermal maturity. *Int. J. Coal Geol.* **2014**, *125*, 1–9. [CrossRef]
31. Maher, K.; Bargar, J.R.; Brown, G.E. Environmental speciation of actinides. *Inorg. Chem.* **2013**, *52*, 3510–3532. [CrossRef] [PubMed]
32. Ray, A.E.; Bargar, J.R.; Sivaswamy, V.; Dohnalkova, A.C.; Fujita, Y.; Peyton, B.M.; Magnuson, T.S. Evidence for multiple modes of uranium immobilization by an anaerobic bacterium. *Geochim. Cosmochim. Acta* **2011**, *75*, 2684–2695. [CrossRef]
33. Wellman, D.M.; Glovack, J.N.; Parker, K.; Richards, E.L.; Pierce, E.M. Sequestration and retention of uranium (VI) in the presence of hydroxylapatite under dynamic geochemical conditions. *Environ. Chem.* **2008**, *5*, 40–50. [CrossRef]
34. Chen, C.S.; Lee, S.F.; Lii, K.H. K(UO)Si_2O_6: A pentavalent-uranium silicate. *J. Am. Chem. Soc.* **2005**, *127*, 12208–12209. [CrossRef] [PubMed]
35. Langmuir, D. Uranium solution-mineral equilibria at low temperatures with applications to sedimentary ore deposits. *Geochim. Cosmochim. Acta* **1978**, *42*, 547–569. [CrossRef]
36. Renshaw, J.C.; Butchins, L.J.C.; Livens, F.R.; May, I.; Charnock, J.M.; Lloyd, J.R. Bioreduction of uranium: Environmental implications of a pentavalent intermediate. *Environ. Sci. Technol.* **2005**, *39*, 5657–5660. [CrossRef] [PubMed]
37. Jones, B.; Manning, D.A.C. Comparison of geochemical indices used for the interpretation of palaeoredox conditions in ancient mudstones. *Chem. Geol.* **1994**, *111*, 111–129. [CrossRef]
38. Bednar, A.; Gent, D.; Gilmore, J.; Sturgis, T.; Larson, S. Mechanisms of thorium migration in a semiarid soil. *J. Environ. Qual.* **2004**, *33*, 2070–2077. [CrossRef]

39. Lieser, K.; Hill, R. Hydrolysis and colloid formation of thorium in water and consequences for its migration behaviour–comparison with uranium. *Radiochim. Acta* **1992**, *56*, 37–46. [CrossRef]
40. Qin, S.; Li, J.; Liang, C.; Zhou, G.; Yuan, M. Helium enrichment mechanism of helium-rich gas reservoirs in central and western china: Degassing and accumulation from ancient groundwater. *J. Nat. Gas Geosci.* **2022**, *7*, 249–264. [CrossRef]
41. Liu, K.; Chen, J.; Tang, S.; Zhang, J.; Fu, R.; Chen, C.; Zou, Y.; Zhang, B.; Wang, H.; Zhang, B. Differential enrichment mechanism of helium in the jinqiu gas field of sichuan basin, china. *Mar. Pet. Geol.* **2024**, *167*, 106970. [CrossRef]
42. Zhang, B.; Zhang, B.; Wang, H.; Chen, J.; Liu, K.; Dou, S.; Dai, X.; Chen, S. The jinqiu gas field in the sichuan basin: A typical helium-bearing to helium-rich gas field with the mesozoic sedimentary rocks as helium source rocks. *Oil Gas Geol.* **2024**, *45*, 185–199. (In Chinese) [CrossRef]
43. Wang, Z.; Liu, J.; Jiang, H.; Huang, S.; Wang, K.; Xu, Z.; Jiang, Q.; Shi, S.; Ren, M.; Wang, T. Lithofacies paleogeography and exploration significance of sinian doushantuo depositional stage in the middle-upper yangtze region, sichuan basin, sw china. *Pet. Explor. Dev.* **2019**, *46*, 41–53. [CrossRef]
44. Li, Y.; Zhang, T.; Ellis, G.S.; Shao, D. Depositional environment and organic matter accumulation of upper ordovician–lower silurian marine shale in the upper yangtze platform, south china. *Palaeogeogr. Palaeoclimatol. Palaeoecol.* **2017**, *466*, 252–264. [CrossRef]
45. Xiao, D.; Cao, J.; Luo, B.; Tan, X.; Xiao, W.; He, Y.; Li, K. Neoproterozoic postglacial paleoenvironment and hydrocarbon potential: A review and new insights from the doushantuo formation sichuan basin, china. *Earth Sci. Rev.* **2021**, *212*, 103453. [CrossRef]
46. Wang, H.; Li, Z.W.; Liu, S.G.; Ran, B.; Song, J.M.; Li, J.X.; Ye, Y.H.; Li, N. Ediacaran extension along the northern margin of the yangtze platform, south china: Constraints from the lithofacies and geochemistry of the doushantuo formation. *Mar. Pet. Geol.* **2020**, *112*, 104056. [CrossRef]
47. Yuan, B.; Dai, X.; Chen, J.; Zhu, H.; Ni, Y. Hydrocarbon generation potential of source rocks of sinian doushantuo formation, sichuan basin and its periphery. *Nat. Gas Explor. Dev.* **2024**, *47*, 1–10. (In Chinese) [CrossRef]
48. Zhu, G.; Zhao, K.; Li, T.; Zhang, Z. Formation mechanism and distribution prediction of source rocks in the ediacaran doushantuo formation, south china. *Acta Geol. Sin.* **2021**, *95*, 2553–2574. (In Chinese) [CrossRef]
49. Luo, Q.; Hao, J.; Skovsted, C.B.; Luo, P.; Khan, I.; Wu, J.; Zhong, N. The organic petrology of graptolites and maturity assessment of the wufeng–longmaxi formations from chongqing, china: Insights from reflectance cross-plot analysis. *Int. J. Coal Geol.* **2017**, *183*, 161–173. [CrossRef]
50. Luo, Q.; Zhong, N.; Wang, Y.; Ma, L.; Li, M. Provenance and paleoweathering reconstruction of the mesoproterozoic hongshuizhuang formation (1.4 Ga), northern north china. *Int. J. Earth Sci.* **2015**, *104*, 1701–1720. [CrossRef]
51. Tribovillard, N.; Algeo, T.J.; Lyons, T.; Riboulleau, A. Trace metals as paleoredox and paleoproductivity proxies: An update. *Chem. Geol.* **2006**, *232*, 12–32. [CrossRef]
52. Taylor, S.R.; McLennan, S.M. The continental crust: Its composition and evolution. *Geol. Mag.* **1985**, *122*, 673–674.
53. Nesbitt, H.; Young, G.M. Early proterozoic climates and plate motions inferred from major element chemistry of lutites. *Nature* **1982**, *299*, 715–717. [CrossRef]
54. Fedo, C.M.; Wayne Nesbitt, H.; Young, G.M. Unraveling the effects of potassium metasomatism in sedimentary rocks and paleosols, with implications for paleoweathering conditions and provenance. *Geology* **1995**, *23*, 921–924. [CrossRef]
55. Harnois, L. The ciw index: A new chemical index of weathering. *Sediment. Geol.* **1988**, *55*, 319–322. [CrossRef]
56. McLennan, S.; Hemming, S.; McDaniel, D.; Hanson, G. Geochemical approaches to sedimentation, provenance, and tectonics. *Geol. Soc. Am. Spec. Pap.* **1993**, *284*, 21–40. [CrossRef]
57. Dang, D.H.; Wang, W.; Gibson, T.M.; Kunzmann, M.; Andersen, M.B.; Halverson, G.P.; Evans, R.D. Authigenic uranium isotopes of late proterozoic black shale. *Chem. Geol.* **2022**, *588*, 120644. [CrossRef]
58. Bau, M.; Dulski, P. Distribution of yttrium and rare-earth elements in the penge and kuruman iron-formations, transvaal supergroup, south africa. *Precambrian Res.* **1996**, *79*, 37–55. [CrossRef]
59. Luo, Q.; Zhang, L.; Zhong, N.; Wu, J.; Goodarzi, F.; Sanei, H.; Skovsted, C.B.; Suchý, V.; Li, M.; Ye, X.; et al. Thermal evolution behavior of the organic matter and a ray of light on the origin of vitrinite-like maceral in the mesoproterozoic and lower cambrian black shales: Insights from artificial maturation. *Int. J. Coal Geol.* **2021**, *244*, 103813. [CrossRef]
60. Wu, J.; Luo, Q.Y.; Zhang, Y.; Zhong, N.N.; Goodarzi, F.; Suchy, V.; Li, M.J.; Li, D.H.; Wang, W.X.; Tian, X.W.; et al. The organic petrology of vitrinite-like maceral in the lower paleozoic shales: Implications for the thermal maturity evaluation. *Int. J. Coal Geol.* **2023**, *274*, 104282. [CrossRef]
61. Gregg, J.M.; Bish, D.L.; Kaczmarek, S.E.; Machel, H.G. Mineralogy, nucleation and growth of dolomite in the laboratory and sedimentary environment: A review. *Sedimentology* **2015**, *62*, 1749–1769. [CrossRef]
62. Murphy, A.E.; Sageman, B.B.; Hollander, D.J.; Lyons, T.W.; Brett, C.E. Black shale deposition and faunal overturn in the devonian appalachian basin: Clastic starvation, seasonal water-column mixing, and efficient biolimiting nutrient recycling. *Paleoceanography* **2000**, *15*, 280–291. [CrossRef]

63. Turgeon, S.; Brumsack, H.-J. Anoxic vs dysoxic events reflected in sediment geochemistry during the cenomanian–turonian boundary event (cretaceous) in the umbria–marche basin of central italy. *Chem. Geol.* **2006**, *234*, 321–339. [CrossRef]
64. Fu, J.H.; Li, S.X.; Xu, L.M.; Niu, X.B. Paleo-sedimentary environmental restoration and its significance of chang 7 member of triassic yanchang formation in ordos basin, nw china. *Petrol. Explor. Dev.* **2018**, *45*, 998–1008. [CrossRef]
65. Wedepohl, D.K.H. Chemical composition and fractionation of the continental crust. *Geol. Rundsch.* **1991**, *80*, 207–223. [CrossRef]
66. Algeo, T.J.; Maynard, J.B. Trace-element behavior and redox facies in core shales of upper pennsylvanian kansas-type cyclothems. *Chem. Geol.* **2004**, *206*, 289–318. [CrossRef]
67. Zheng, Y.; Anderson, R.F.; Van Geen, A.; Kuwabara, J. Authigenic molybdenum formation in marine sediments: A link to pore water sulfide in the santa barbara basin. *Geochim. Cosmochim. Acta* **2000**, *64*, 4165–4178. [CrossRef]
68. Tribovillard, N.; Algeo, T.J.; Baudin, F.; Riboulleau, A. Analysis of marine environmental conditions based onmolybdenum–uranium covariation—Applications to mesozoic paleoceanography. *Chem. Geol.* **2012**, *324–325*, 46–58. [CrossRef]
69. Qiao, J.; Littke, R.; Grohmann, S.; Zhang, C.; Jiang, Z.; Strauss, H.; Zieger, L. Climatic and environmental conditions during the pleistocene in the central qaidam basin, ne tibetan plateau: Evidence from gdgts, stable isotopes and major and trace elements of the qigequan formation. *Int. J. Coal Geol.* **2022**, *254*, 103958. [CrossRef]
70. Huerta-Diaz, M.A.; Morse, J.W. Pyritization of trace metals in anoxic marine sediments. *Geochim. Cosmochim. Acta* **1992**, *56*, 2681–2702. [CrossRef]
71. Schoepfer, S.D.; Shen, J.; Wei, H.; Tyson, R.V.; Ingall, E.; Algeo, T.J. Total organic carbon, organic phosphorus, and biogenic barium fluxes as proxies for paleomarine productivity. *Earth Sci. Rev.* **2015**, *149*, 23–52. [CrossRef]
72. Dymond, J. Geochemistry of nazca plate surface sediments: An evaluation of hydrothermal, biogenic, detrital, and hydrogenous sources. In *Nazca Plate: Crustal Formation and Andean Convergence*; Geological Society of America: Boulder, CO, USA, 1981. [CrossRef]
73. Dymond, J.; Suess, E.; Lyle, M. Barium in deep-sea sediment: A geochemical proxy for paleoproductivity. *Paleoceanography* **1992**, *7*, 163–181. [CrossRef]
74. Calvert, S.E.; Pedersen, T.F. Chapter fourteen elemental proxies for palaeoclimatic and palaeoceanographic variability in marine sediments: Interpretation and application. In *Developments in Marine Geology*; Hillaire-Marcel, C., De Vernal, A., Eds.; Elsevier: Amsterdam, The Netherlands, 2007; Volume 1, pp. 567–644. [CrossRef]
75. Yu, W.; Tian, J.; Wang, F.; Liang, Q.; Yang, T.; Kneller, B.; Liang, X. Sedimentary environment and organic matter enrichment of black mudstones from the upper triassic chang-7 member in the ordos basin, northern china. *J. Asian Ear. Sci.* **2022**, *224*, 105009. [CrossRef]
76. Sun, W.-H.; Zhou, M.-F.; Yan, D.-P.; Li, J.-W.; Ma, Y.-X. Provenance and tectonic setting of the neoproterozoic yanbian group, western yangtze block (SW China). *Precambrian Res.* **2008**, *167*, 213–236. [CrossRef]
77. Hayashi, K.I.; Fujisawa, H.; Holland, H.D.; Ohmoto, H. Geochemistry of approximately 1.9 Ga sedimentary rocks from northeastern labrador, Canada. *Geochim. Cosmochim. Acta* **1997**, *61*, 4115–4137. [CrossRef]
78. Wang, L.J.; Griffin, W.L.; Yu, J.H.; O'Reilly, S.Y. U–Pb and Lu–Hf isotopes in detrital zircon from neoproterozoic sedimentary rocks in the northern yangtze block: Implications for precambrian crustal evolution. *Gondwana Res.* **2013**, *23*, 1261–1272. [CrossRef]
79. Zhang, S.B.; Zheng, Y.F.; Zhao, Z.F.; Wu, Y.B.; Yuan, H.l.; Wu, F.Y. Neoproterozoic anatexis of archean lithosphere: Geochemical evidence from felsic to mafic intrusions at xiaofeng in the Yangtze Gorge, South China. *Precambrian Res.* **2008**, *163*, 210–238. [CrossRef]
80. Hu, R. Geochemical Characteristics and Implications of the Nantuo and Doushantuo Formations in the Three Gorges Area. Ph.D. Thesis, University of Science and Technology of China, Hefei, China, 2017. (In Chinese).
81. Qiu, X.; Yang, H.; Zhao, X.; Lu, S.; Jiang, T.; Duan, R.; Liu, C.; Peng, L.; Wei, Y. Neoarchean granitic gneisses in the kongling complex, yangtze craton: Petrogenesis and tectonic implications. *Earth Sci.* **2019**, *44*, 415–426. (In Chinese) [CrossRef]
82. Wang, X.; Ossa Ossa, F.; Hofmann, A.; Agangi, A.; Paprika, D.; Planavsky, N.J. Uranium isotope evidence for mesoarchean biological oxygen production in shallow marine and continental settings. *Earth Planet. Sci. Lett.* **2020**, *551*, 116583. [CrossRef]
83. Zheng, Y.; Anderson, R.F.; van Geen, A.; Fleisher, M.Q. Remobilization of authigenic uranium in marine sediments by bioturbation. *Geochim. Cosmochim. Acta* **2002**, *66*, 1759–1772. [CrossRef]
84. Dai, S.; Ren, D.; Chou, C.-L.; Finkelman, R.B.; Seredin, V.V.; Zhou, Y. Geochemistry of trace elements in chinese coals: A review of abundances, genetic types, impacts on human health, and industrial utilization. *Int. J. Coal Geol.* **2012**, *94*, 3–21. [CrossRef]
85. Humphris, S.E.; Thompson, G. Trace element mobility during hydrothermal alteration of oceanic basalts. *Geo Chim. Cosmochim. Acta* **1978**, *42*, 127–136. [CrossRef]
86. Liu, Q.; Zhu, D.; Jin, Z.; Meng, Q.; Li, S. Influence of volcanic activities on redox chemistry changes linked to the enhancement of the ancient sinian source rocks in the Yangtze craton. *Precambrian Res.* **2019**, *327*, 1–13. [CrossRef]
87. Cullers, R.L. Implications of elemental concentrations for provenance, redox conditions, and metamorphic studies of shales and limestones near Pueblo, Co, USA. *Chem. Geol.* **2002**, *191*, 305–327. [CrossRef]

88. Pan, Y.M.; Fleet, M.E. Compositions of the apatite-group minerals: Substitution mechanisms and controlling factors. In *Phosphates: Geochemical, Geobiological and Materials Importance*; Kohn, M.J., Rakovan, J., Hughes, J.M., Eds.; Mineralogical Society of America: Washington, DC, USA, 2002; Volume 48, pp. 13–49. [CrossRef]
89. Bonnetti, C.; Cuney, M.; Malartre, F.; Michels, R.; Liu, X.D.; Peng, Y.B. The nuheting deposit, erlian basin, ne china: Synsedimentary to diagenetic uranium mineralization. *Ore Geol. Rev.* **2015**, *69*, 118–139. [CrossRef]
90. Meunier, J.D.; Trouiller, A.; Brulhet, J.; Pagel, M. Uranium and organic matter in a paleodeltaic environment: The coutras deposit (Gironde, France). *Chem. Geol.* **1988**, *70*, 189. [CrossRef]
91. Regenspurg, S.; Margot-Roquier, C.; Harfouche, M.; Froidevaux, P.; Steinmann, P.; Junier, P.; Bernier-Latmani, R. Speciation of naturally-accumulated uranium in an organic-rich soil of an alpine region (Switzerland). *Geochim. Cosmochim. Acta* **2010**, *74*, 2082–2098. [CrossRef]
92. Gad, N.S.; Mousa, D.A.; Makled, W.A.; Gentzis, T.; Samaan, J. Biosorption of some elements by algae from a cutinite-rich coal and its effect on organic geochemical composition: A case study from Abu Thora, Sinai, Egypt. *Int. J. Coal Geol.* **2023**, *270*, 104231. [CrossRef]
93. Wang, M.; Wu, B.; Li, Y.; Liu, C.; Hao, X.; Liu, M.; Zhang, W.; Li, Q.; Yao, L.; Zhang, X. Experimental study on possibility of deep uranium-rich source rocks providing uranium source in ordos basin. *Earth Sci.* **2022**, *47*, 224–239. (In Chinese) [CrossRef]
94. Qiu, L.F.; Wu, Y.; Wang, Q.; Wu, L.F.; He, Z.B.; Peng, S.; Fan, Y.F. Metallogenic mechanism of typical carbonate-hosted uranium deposits in Guizhou (China). *Minerals* **2022**, *12*, 585. [CrossRef]
95. Ramasamy, V.; Suresh, G.; Meenakshisundaram, V.; Ponnusamy, V. Horizontal and vertical characterization of radionuclides and minerals in river sediments. *Appl. Radiat. Isot.* **2011**, *69*, 184–195. [CrossRef] [PubMed]
96. Ramasamy, V.; Paramasivam, K.; Suresh, G.; Jose, M.T. Function of minerals in the natural radioactivity level of vaigai river sediments, tamilnadu, india—Spectroscopical approach. *Spectrochim. Acta Part A Mol. Biomol. Spec.* **2014**, *117*, 340–350. [CrossRef] [PubMed]
97. Ifeoma Mary, U.; Onyedikachi Anthony, I. Sorption of heavy metals on clay minerals and oxides: A review. In *Advanced Sorption Process Applications*; Serpil, E., Ed.; IntechOpen: Rijeka, Croatia, 2019; p. 7. [CrossRef]
98. Yin, Z.X.; Pan, D.Q.; Liu, P.; Wu, H.Y.; Li, Z.; Wu, W.S. Sorption behavior of thorium(IV) onto activated bentonite. *J. Radio. Nucl. Chem.* **2018**, *316*, 301–312. [CrossRef]
99. Yusof, M.Y.M.; Idris, M.I.; Mohamed, F.; Nor, M.M. Adsorption of radioactive element by clay: A review. In *IOP Conference Series: Materials Science and Engineering*; IOP Publishing: Bristolb, UK, 2020; p. 012020. [CrossRef]
100. Wang, X.; Li, S.; Huang, Z.; Li, P.; Wang, X. The sorption behavior of Th(IV)on kaolinite. *Chem. Res. Appl.* **2016**, *28*, 738–742. (In Chinese)
101. Zhang, B.; Zhang, S. Metallogenic characteristics and geological exploration of thorium deposits. *World Nuclear Geosci.* **2005**, *4*, 203–210. (In Chinese)
102. Zhao, C.; Liu, B.; Xiao, L.; Li, Y.; Liu, S.; Li, Z.; Zhao, B.; Ma, J.; Chu, G.; Gao, P.; et al. Significant enrichment of Ga, Rb, Cs, REEs and Y in the jurassic no. 6 coal in the iqe Coalfield, northern Qaidam Basin, China—A hidden gem. *Ore Geol. Rev.* **2017**, *83*, 1–13. [CrossRef]
103. Ward, C.R.; Spears, D.A.; Booth, C.A.; Staton, I.; Gurba, L.W. Mineral matter and trace elements in coals of the Gunnedah Basin, New South Wales, Australia. *Int. J. Coal Geol.* **1999**, *40*, 281–308. [CrossRef]
104. Seredin, V.V. Anomalous concentrations of trace elements in the spetsugli germanium deposit (pavlovka brown coal deposit, southern primorye): Communication 2. Rubidium and cesium. *Lithol. Miner. Resour.* **2003**, *38*, 233–241. [CrossRef]
105. Swaine, D.J. *Trace Elements in Coal*; Butterworth-Heinemann: Oxford, UK, 2013.
106. Wang, J.; Xiao, S.; Du, Q.; Zhou, G.; Wang, T.; Li, Q.; Fu, X.; Wei, H.; He, Y.; Shen, L. Paleomarine environment and organic matter enrichment mechanism of doushantuo black shale in the northeastern Sichuan Basin. *Nat. Gas Ind.* **2023**, *43*, 76–92. (In Chinese) [CrossRef]
107. Wang, W.; Xiao, W.; He, Y.; Zuo, Z.; Deng, S.; Cao, J. Geochemical characteristics of the sinian doushantuo formation source rocks of the Sichuan Basin: Implications for the organic matter accumulation. *Geol. J. China Univer.* **2019**, *25*, 860–870. (In Chinese) [CrossRef]
108. Jiang, G.; Shi, X.; Zhang, S.; Wang, Y.; Xiao, S. Stratigraphy and paleogeography of the ediacaran doushantuo formation (ca. 635–551ma) in South China. *Gondwana Res.* **2011**, *19*, 831–849. [CrossRef]
109. Nie, H.; Jin, Z.; Li, P.; Jay Katz, B.; Dang, W.; Liu, Q.; Ding, J.; Jiang, S.; Li, D. Deep shale gas in the ordovician-silurian wufeng–longmaxi formations of the Sichuan Basin, SW China: Insights from reservoir characteristics, preservation conditions and development strategies. *J. Asian Earth Sci.* **2023**, *244*, 105521. [CrossRef]
110. Zhao, J.; Jin, Z.; Jin, Z.; Wen, X.; Geng, Y.; Yan, C.; Nie, H. Depositional environment of shale in wufeng and longmaxi formations, Sichuan Basin. *Pet. Res.* **2017**, *2*, 209–221. [CrossRef]

111. Ge, X.; Mou, C.; Yu, Q.; Liu, W.; Men, X.; He, J. The geochemistry of the sedimentary rocks from the huadi no. 1 well in the wufeng-longmaxi formations (upper ordovician-lower silurian), South China, with implications for paleoweathering, provenance, tectonic setting and paleoclimate. *Mar. Pet. Geol.* **2019**, *103*, 646–660. [CrossRef]
112. Yan, C.; Jin, Z.; Zhao, J.; Du, W.; Liu, Q. Influence of sedimentary environment on organic matter enrichment in shale: A case study of the wufeng and longmaxi formations of the Sichuan Basin, China. *Mar. Pet. Geol.* **2018**, *92*, 880–894. [CrossRef]
113. Zhang, L.; Xiao, D.; Lu, S.; Jiang, S.; Lu, S. Effect of sedimentary environment on the formation of organic-rich marine shale: Insights from major/trace elements and shale composition. *Int. J. Coal Geol.* **2019**, *204*, 34–50. [CrossRef]
114. Meng, B.; Li, J.; Zhou, S.; Dan, Y.; Zhang, Q.; Nie, G. Origin and source of helium in the resolved gas of sinian-cambrian shale in the qiannan depression. *Nat. Gas Geosci.* **2023**, *34*, 647–655. (In Chinese) [CrossRef]
115. Yang, Y.; Wen, L.; Luo, B.; Song, J.; Chen, X.; Wang, X.; Hong, H.; Zhou, G.; He, Q.; Zhang, X.; et al. Sedimentary tectonic evolution and reservoir-forming conditions of the dazhou–kaijiang paleo-uplift, Sichuan Basin. *Nat. Gas Ind. B* **2016**, *3*, 515–525. [CrossRef]